The Deep Equatorial Ocean Circulation in Wind-Forced Numerical Solutions*

FRANÇOIS ASCANI

Marine Science Department, University of Hawai'i at Hilo, Hilo, Hawaii

ERIC FIRING

School of Ocean and Earth Science and Technology, Department of Oceanography, University of Hawai'i at Mānoa, Honolulu, Hawaii

JULIAN P. MCCREARY

Department of Oceanography, School of Ocean and Earth Science and Technology, and International Pacific Research Center, University of Hawai'i at Mānoa, Honolulu, Hawaii

PETER BRANDT AND RICHARD J. GREATBATCH

GEOMAR Helmholtz-Zentrum für Ozeanforschung Kiel, Kiel, Germany

(Manuscript received 7 August 2014, in final form 6 April 2015)

ABSTRACT

We perform eddy-resolving and high vertical resolution numerical simulations of the circulation in an idealized equatorial Atlantic Ocean in order to explore the formation of the deep equatorial circulation (DEC) in this basin. Unlike in previous studies, the deep equatorial intraseasonal variability (DEIV) that is believed to be the source of the DEC is generated internally by instabilities of the upper-ocean currents. Two main simulations are discussed: solution 1, configured with a rectangular basin and with wind forcing that is zonally and temporally uniform, and solution 2, with realistic coastlines and an annual cycle of wind forcing varying zonally. Somewhat surprisingly, solution 1 produces the more realistic DEC; the large, vertical-scale currents [equatorial intermediate currents (EICs)] are found over a large zonal portion of the basin, and the small, vertical-scale equatorial currents [equatorial deep jets (EDJs)] form low-frequency, quasi-resonant, baroclinic equatorial basin modes with phase propagating mostly downward, consistent with observations. This study demonstrates that both types of currents arise from the rectification of DEIV, consistent with previous theories. The authors also find that the EDJs contribute to maintaining the EICs, suggesting that the nonlinear energy transfer is more complex than previously thought. In solution 2, the DEC is unrealistically weak and less spatially coherent than in the first simulation probably because of its weaker DEIV. Using intermediate solutions, this study finds that the main reason for this weaker DEIV is the use of realistic coastlines in solution 2. It remains to be determined what needs to be modified or included to obtain a realistic DEC in the more realistic configuration.

1. Introduction

a. Overview

The equatorial Atlantic and Pacific Oceans exhibit a complex set of zonal currents at intermediate depths (500–2500 m), typically with an instantaneous amplitude of up to 15–25 cm s^{-1} (Fig. 1; Firing 1987; Schott et al. 1995, 2003; Firing et al. 1998; Gouriou et al. 1999,

* International Pacific Research Center Publication Number 1116 and School of Ocean and Earth Science and Technology Publication Number 9400.

Corresponding author address: François Ascani, Marine Science Department, University of Hawai'i at Hilo, 200 W. Kawili St., Hilo, HI 96720.
E-mail: fascani@hawaii.edu

DOI: 10.1175/JPO-D-14-0171.1

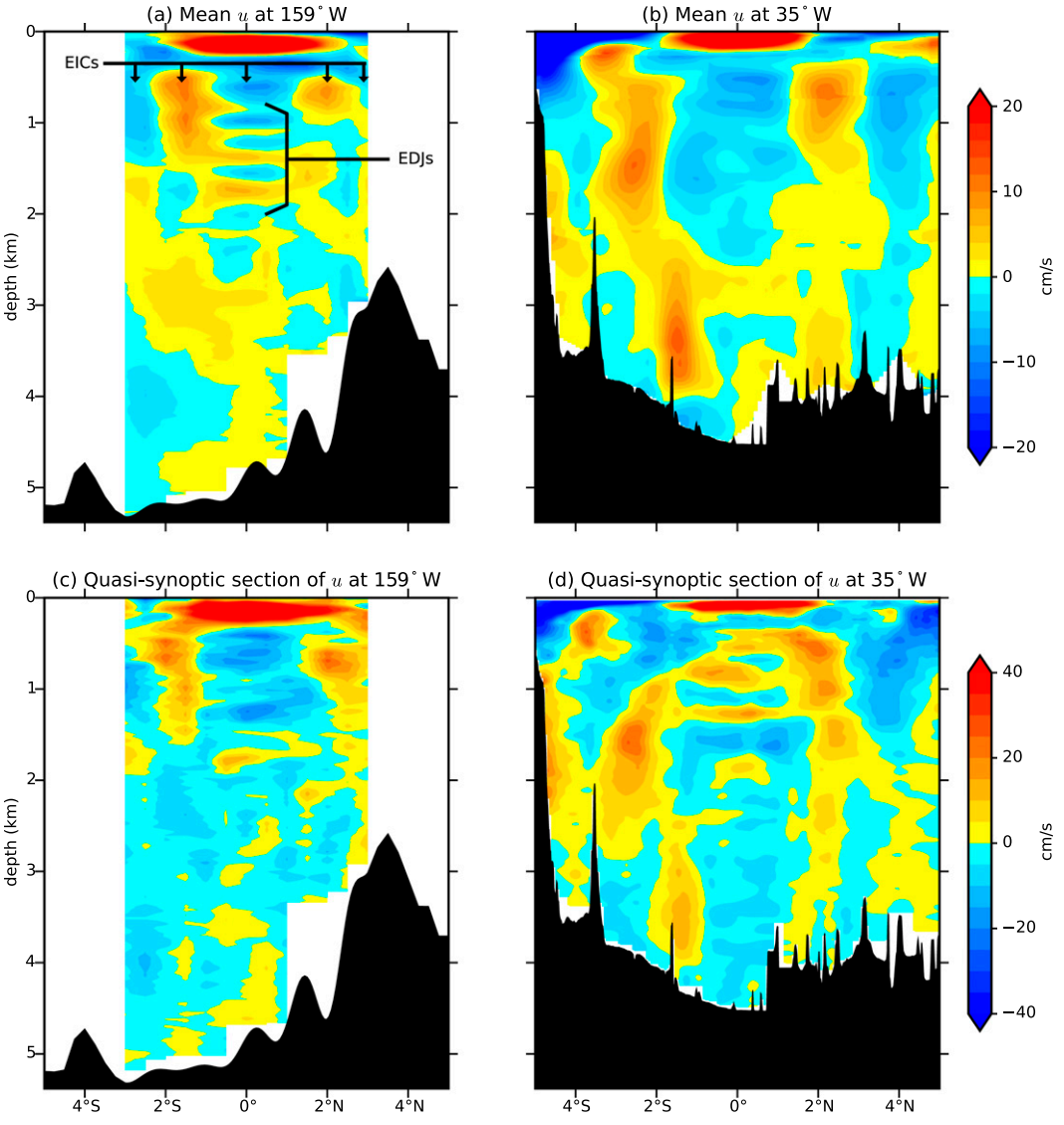

FIG. 1. (a) Mean zonal component of velocity u from shipboard observations at 159°W (21 cruises between March 1982 and June 1983; see Firing 1987). (b) Mean u from shipboard observations at 35°W (10 cruises between 1990 and 2003; see Eden and Dengler 2008). (c) A quasi-synoptic section of u out of the dataset at 159°W (May–June 1982). (d) A quasi-synoptic section of u out of the dataset at 35°W (May 2003). Notice the different color scale for the quasi-synoptic sections and the means. The EDJs do not appear in (b) because the time span of measurements used for the average (~13 yr) is 2 to 3 times longer that the period of the EDJs (5 ± 1 yr; Johnson and Zhang 2003).

2001; Bourlès et al. 2002, 2003; Send et al. 2002; Ollitrault et al. 2006; Eden and Dengler 2008; Ascani et al. 2010; Brandt et al. 2011, 2012; Cravatte et al. 2012; Youngs and Johnson 2015, manuscript submitted to *J. Phys. Oceanogr.*). This deep equatorial circulation (DEC; see a list of abbreviations in Table 1) is composed of two types of flow: equatorial deep jets (EDJs), which are trapped at the equator and alternate with depth with a vertical wavelength of about 400–600 m, and equatorial intermediate currents (EICs), which have a large vertical scale and alternate with latitude every 1°–2° between about 5°S and 5°N.[1]

Both sets of currents contribute to the global ocean circulation and the zonal distribution of water masses

[1] Latitudinally alternating, large, vertical-scale zonal jets are also found at more poleward latitudes [see Ollitrault et al. (2006), Cravatte et al. (2012), and Qiu et al. (2013) for a recent account]. We do not include them in the present paper but note that the dynamical similarity between these jets and the EICs is still unclear.

TABLE 1. List of abbreviations for currents and ocean motions used in the text.

Abbreviation	Meaning
DEC	Deep equatorial circulation
DWBC	Deep western boundary current
DEIV	Deep equatorial intraseasonal variability
EDJs	Equatorial deep jets
EICs	Equatorial intermediate currents
LEIC	Lower Equatorial Intermediate Current
MRG	Mixed Rossby–gravity
NBC	North Brazil Current
NECC	North Equatorial Countercurrent
NEIC	North Equatorial Intermediate Current
NICC	North Intermediate Countercurrent
SEC	South Equatorial Current
SEIC	South Equatorial Intermediate Current
SICC	South Intermediate Countercurrent
TIWs	Tropical instability waves

and biogeochemical quantities. For instance, the eastward jets have been shown to supply dissolved oxygen to the oxygen minimum zone of the deep eastern equatorial Atlantic and Pacific Oceans (Stramma et al. 2005; Eden 2006; Brandt et al. 2008; Stramma et al. 2010; Czeschel et al. 2011; Brandt et al. 2012). Further, the large-scale biases in the nutrient and oxygen fields in global, coupled, biogeochemical ocean models have been attributed to inaccuracies of the simulated DEC (Dietze and Loeptien 2013; Getzlaff and Dietze 2013). Finally, Brandt et al. (2011) provide evidence that the upward-propagating energy and interannual variability of the EDJs in the Atlantic Ocean might be indirectly responsible for a portion of the interannual atmospheric variability via their modulation of sea surface temperature (SST).

On the modeling side, a realistic DEC is absent in most ocean general circulation model (OGCM) solutions. At the same time, recent theory and idealized numerical simulations have shown that the DEC may arise from the rectification of the deep equatorial intraseasonal variability (DEIV) (d'Orgeville et al. 2007; Hua et al. 2008; Ménesguen et al. 2009; Ascani et al. 2010). The reasons for this inconsistency are not clear. One possible cause is that DEIV, which arises internally from instabilities of the mean circulation in OGCMs, may be poorly reproduced in these models.

b. Present research

In this study, we continue the effort to understand DEC dynamics and improve its modeling; for this purpose, we focus on the Atlantic Ocean. Specifically, we seek to reduce the gap between idealized and OGCM simulations by obtaining a series of numerical solutions that generate DEIV internally. We have tested many configurations with varying parameters and degrees of realism. Here, we focus on two: solution 1, with a rectangular basin and with winds varying only with latitude, and solution 2, with realistic coastlines and an annual cycle of zonally and meridionally varying winds based on Atlantic climatology. We also briefly mention the results of two intermediate solutions (solutions 1.5 and 1.8) to understand the differences between solutions 1 and 2. In all solutions, instabilities of the upper-ocean mean equatorial circulation, known as tropical instability waves (TIWs), provide the source for DEIV, and a DEC with some resemblance to Atlantic observations is obtained. Surprisingly, the more realistic DEC is obtained in the more idealized simulation (solution 1). In particular, the EICs are found over a large zonal portion of the basin, and the EDJs form low-frequency, quasi-resonant, baroclinic equatorial basin modes with the phase propagating mostly downward, consistent with observations. We then study DEC dynamics by analyzing the zonal kinetic energy budget in solution 1. We confirm the results of previous studies that DEIV is the original source for DEC, but we also discover that the EDJs supply energy to the EICs, suggesting that the nonlinear energy transfer involved in the formation of DEC is more complex than previously assumed.

The paper is organized as follows: Section 2 provides a background for our study, reviewing the temporal and spatial characteristics of the EDJs and EICs in both the Pacific and Atlantic Oceans, their simulation in previous idealized and realistic numerical models, and the theories proposed to explain them. Section 3 describes the overall design of our modeling experiments. Section 4 describes the upper-ocean circulation, DEIV, and DEC in solutions 1 and 2, noting the similarity of the modeled EDJs to low-frequency, baroclinic, equatorial basin modes. The results of the two intermediate solutions are also discussed. Section 5 discusses the dynamical processes that link DEIV to the DEC via the analysis of the zonal kinetic energy budget. Section 6 provides a summary and discussion of our results, including implications of the differences between solutions 1 and 2 for the modeling of DEC in OGCMs.

2. Background

In this section, we review the temporal and spatial structure of observed EDJs and EICs, their reproduction in previous numerical models, and the theories proposed to explain them.

a. Observations

Multiyear collections of CTD and horizontal velocity data in the Atlantic Ocean provide information on the

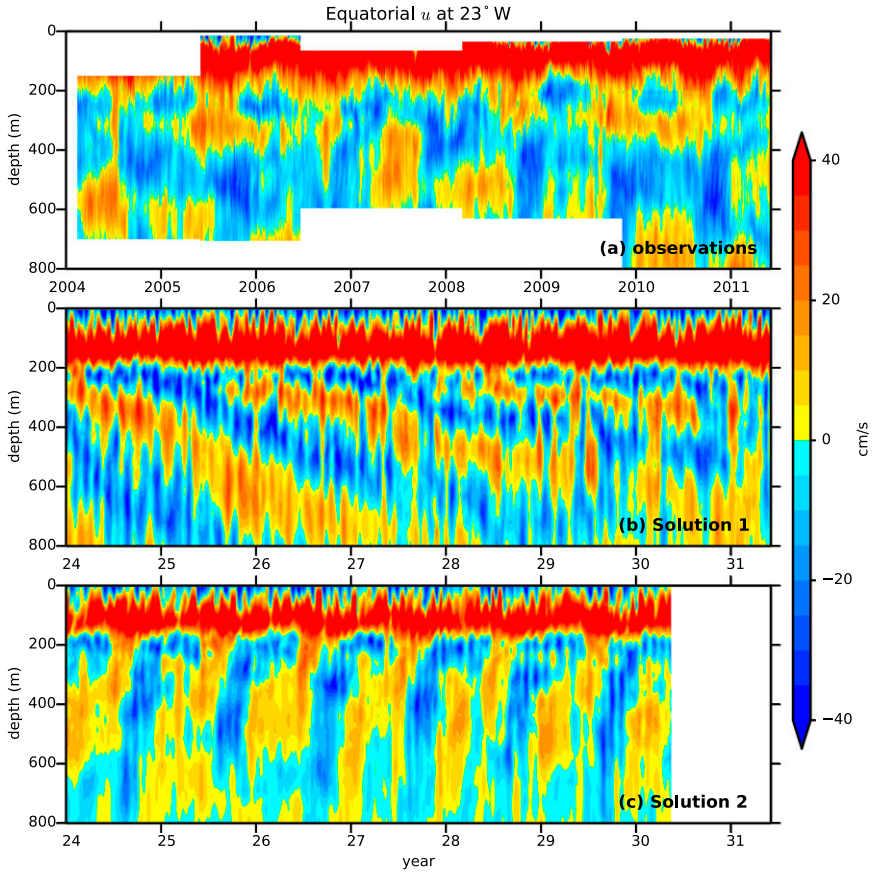

FIG. 2. Time series of equatorial u at 23°W in (a) the observations of Brandt et al. (2011, 2012), (b) solution 1, and (c) solution 2.

spatial and temporal characteristics of the EDJs and on their underlying dynamics. Johnson and Zhang (2003) analyzed the EDJ signature in the vertical strain of density from all available CTD data collected in the Atlantic Ocean, a dataset that spanned about 25 yr. They concluded that the Atlantic EDJs have a period of about 5 ± 1 yr and exhibit downward phase propagation; consistent with linear equatorial wave theory, the latter property implies upward energy propagation, suggesting that the origin of the EDJs lies in the deep ocean. These properties have been confirmed recently in an 8-yr time series of horizontal velocity, obtained from moored measurements (reproduced here in Fig. 2a), from horizontal velocity observations spanning several decades derived from the net displacement of profiling floats (Brandt et al. 2011) and, more recently, from an extensive dataset of Argo and shipboard vertical density profiles (Youngs and Johnson 2015, manuscript submitted to *J. Phys. Oceanogr.*).

The relatively long period and small vertical wavelength of the EDJs are consistent with a dynamical description of the Atlantic EDJs in terms of quasi-resonant, low-frequency, baroclinic, equatorial basin modes (Cane and Moore 1981; d'Orgeville et al. 2007; Bunge et al. 2008; Brandt et al. 2011, 2012). These modes are composed principally of a Kelvin wave and its reflection into a first meridional–mode long Rossby wave, with the period of the mode (T_n) being a function of the gravity wave phase speed of the particular baroclinic mode (c_n):

$$T_n = \frac{4L_B}{c_n}, \tag{1}$$

where L_B is the width of the basin. The smaller the vertical wavelength, the lower the gravity wave speed and hence the longer the period of the mode. For the Atlantic Ocean ($L_B \sim 60°$), the basin mode associated with vertical modes 14–16 (~600-m vertical wavelength; $c_n \sim 20\,\mathrm{cm\,s^{-1}}$) has a period of about 4.2 yr, which matches approximately the observed EDJ period. This dynamical interpretation in terms of basin modes is also consistent with the observed meridional structure of the EDJs (Johnson and Zhang 2003; Greatbatch et al. 2012).

In the Pacific Ocean, Firing (1987) observed the EDJs over a 16-month period and did not find any significant vertical migration. Johnson et al. (2002), however, analyzed the signature of the EDJs in the vertical strain of density in the Pacific Ocean, a dataset that spanned about 22 yr. In the eastern Pacific, they found downward phase propagation at a rate suggesting a period of 30 ± 4 yr but noted that inferring periodicity from this dataset is a "dangerous exercise." In both Firing (1987) and Johnson et al. (2002), the EDJs corresponded to about vertical mode 32 ($c_n \sim 10\,\mathrm{cm\,s^{-1}}$); with the Pacific Ocean being about 140° wide, a basin mode with this vertical scale should have a period of about 20 yr, marginally less than Johnson et al.'s (2002) estimate. Youngs and Johnson (2015, manuscript submitted to *J. Phys. Oceanogr.*) recently analyzed an updated dataset, including 4 yr of relatively dense sampling by high-resolution Argo profiles in the Pacific. They found that the EDJ signal in the Pacific is much weaker in amplitude and broader in bandwidth than that in the Atlantic, making it more difficult to identify a single dominant periodic structure. Nevertheless, they isolated basin-scale zonal and temporal coherence of 1.5° on either side of the equator centered at a vertical scale corresponding to mode 22 ($c_n \sim 15\,\mathrm{cm\,s^{-1}}$). The phase propagation was downward and to the west, fitting a first meridional mode Rossby wave with a period of 12 ± 5 yr; for comparison, the period of a basin mode with the same vertical scale is 13 yr.[2]

Unlike the EDJs, the EICs are quasi-steady zonal currents that have been observed consistently from direct velocity measurements (Firing 1987; Firing et al. 1998; Gouriou et al. 2001; Schott et al. 1998, 2003; Brandt et al. 2008) and from the displacements of floats (Ollitrault et al. 2006; Ascani et al. 2010; Cravatte et al. 2012; Ollitrault and Colin de Verdière 2014). Most prominently, they include (Fig. 1) a westward jet located at the equator, referred to in the literature as the Lower Equatorial Intermediate Current (LEIC); two eastward jets that flank the LEIC near 1.5°–2° from the equator, referred to as the North and South Intermediate Countercurrents (NICC and SICC); and a pair of westward jets, 3°–4° from the equator, known as the North and South Equatorial Intermediate Currents (NEIC and SEIC). Remarkably, the EICs extend across almost the entire width of the Atlantic and Pacific Oceans (Fig. 3a).

[2] Although zonal flows described as EDJs were initially observed in the Indian Ocean (Luyten and Swallow 1976), there have not been enough subsequent observations for a clear picture of EDJ behavior based on velocity profiles. From their analysis of vertical strain, Youngs and Johnson (2015, manuscript submitted to *J. Phys. Oceanogr.*) have inferred relatively weak EDJs with a 5-yr period.

b. Models

The EDJs are reproduced inconsistently in eddy-resolving ocean OGCMs of the Atlantic and Pacific Oceans partly, but not entirely, because of inadequate horizontal and vertical resolution (Ascani 2005; Eden and Dengler 2008). To our knowledge, they have been obtained only in one set of simulations of the Atlantic Ocean (Eden and Dengler 2008) and in the Pacific sector of the global simulation described by Ishida et al. (1998) (see Ascani 2005). In both cases, the modeled EDJs are associated with the instability of a deep cross-equatorial current along the western boundary, and their energy propagates horizontally into the interior via Kelvin waves with little or no reflection into long Rossby waves. Hence, unlike in the observations, they do not exhibit vertical propagation nor do they form low-frequency basin modes. With respect to the EICs, they are reproduced in numerical models with sufficient horizontal resolution, but they do not extend as deep as in the observations (Ascani 2005; Eden 2006; Ascani et al. 2010).

c. Theories

Hua et al. (2008) studied numerically and analytically the stability of a short,[3] low baroclinic mode mixed Rossby–gravity (MRG) wave and showed how this wave can rectify into low-frequency motions resembling the EICs and the EDJs. The initial-value problem is addressed in the configuration of a long zonal channel; in this case, a zonally confined packet of MRG waves destabilizes into EIC-like currents that propagate to the west and EDJ-like currents that propagate to the east of the packet. The vertical scale of the EDJs is a function of the zonal wavenumber (or, equivalently, the period) of the MRG wave, such that the shorter the wave, the longer its period and the shorter the vertical scale of the EDJs. For a zonal wavelength of about 3°, period of about 60 days, and wave amplitude of about $30\,\mathrm{cm\,s^{-1}}$, a stacked set of equatorial currents with a vertical wavelength of about 400 m is generated.

Hua et al. (2008) also studied the steady problem in the configuration of a basin with a MRG wave forced at the equator along the western boundary, a process mimicking the instabilities associated with the equatorial crossing of the deep western boundary current (DWBC) in the Atlantic Ocean. In this case (which is more thoroughly studied by d'Orgeville et al. 2007),

[3] Hereinafter, "short" refers to the zonal wavelength and identifies Rossby waves with eastward group velocity and MRG waves with westward phase velocity.

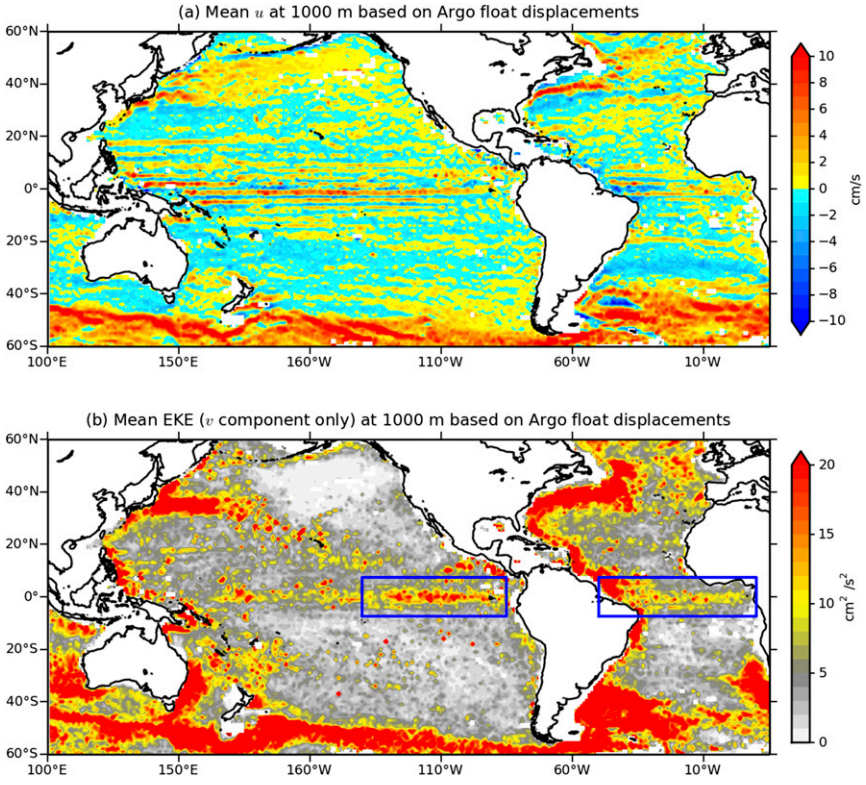

FIG. 3. (a) Mean (1997–2014) u at 1000 m from the net displacements of Argo floats at their parking depth, using the YoMaHa product (Lebedev et al. 2007; Ascani et al. 2010). (b) Mean EKE from the v component only [i.e., $1/2\langle(v-\langle v\rangle)^2\rangle$ where the angle brackets indicate the 1997–2014 mean] from the same dataset. The quantities have been calculated over a $1^\circ \times 1^\circ$ grid. There are about 10 samples per bin on average, and white bins have no observations. Blue frames in (b) indicate regions of DEIV.

EDJ-like currents are also generated, propagating into the interior and forming low-frequency equatorial basin modes. In this scenario, the vertical scale of the EDJs does not depend on the basin width, so the appearance of the EDJs as basin modes does not appear to be essential to the theory. EIC-like currents also appear but only within a few degrees from the western boundary, inconsistent with the Atlantic observations.

To remedy this discrepancy, Ménesguen et al. (2009) explore the case where the forcing is still along the western boundary but is now confined to the upper 2500 m—instead of appearing as a single baroclinic mode. In this case, the forcing excites not only the short low baroclinic mode MRG waves but also short barotropic equatorial Rossby waves. The MRG waves generate EDJs that form basin modes, while the short barotropic Rossby waves generate EICs over a large zonal portion of the basin, as in the observations.

The scenario of d'Orgeville et al. (2007) and Ménesguen et al. (2009), schematized in Fig. 4a, is appealing in that it reproduces currents resembling EDJs and EICs in structure and amplitude and that the EDJs form basin modes. One difference from the observations, however, concerns the observed vertical propagation of the EDJs; the phase of the EDJs propagates both upward and downward in the simulation of d'Orgeville et al. (2007), while it propagates dominantly downward in the observations (Fig. 2a). Another issue concerns the zonal extent of the EICs, which depends critically on how far the short barotropic Rossby waves can propagate into the interior ocean before they become unstable and lose their energy to the EICs. Although the decay might not pose a problem for the narrower Atlantic Ocean, it does for the broader Pacific; for the short Rossby waves to cover a large fraction of the Pacific basin before becoming unstable, they would have to be very weak, in which case little energy is available for generating basinwide EICs.

A second scenario for producing EICs over a long zonal extent has been proposed by Ascani et al. (2010). Instead of DEIV being generated along the western boundary by instabilities of a DWBC, Ascani et al. (2010) propose that the DEIV is generated by the

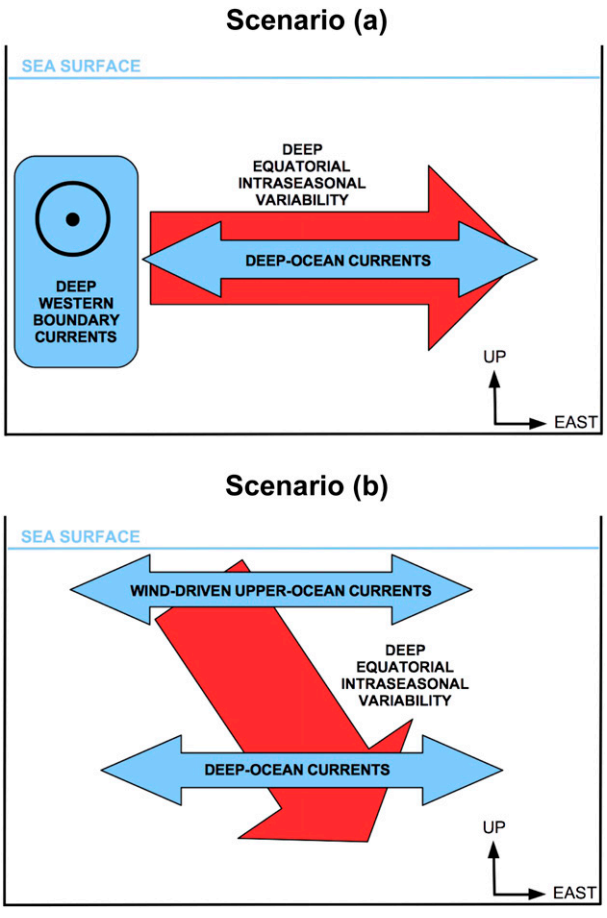

FIG. 4. Two scenarios proposed for the generation of the DEC in the Atlantic Ocean. Both involve the rectification of DEIV. In scenario (a), proposed by d'Orgeville et al. (2007) and Ménesguen et al. (2009) and built on the work of Hua et al. (2008), DEIV is generated directly at depth by the instability of the DWBC crossing the equator. In scenario (b), proposed by Ascani et al. (2010), DEIV is generated away from the western boundary by the instability of the wind-driven upper-ocean circulation, such as TIWs. The red arrows indicate the main direction of DEIV energy propagation in each scenario.

instabilities of the upper-ocean equatorial current system, in particular those associated with TIWs (Fig. 4b). As seen in the realistic simulation analyzed by von Schuckmann et al. (2008) and in the observations and realistic simulations reviewed by Ascani et al. (2010), a large fraction of TIW energy radiates into the deep ocean as a downward- and eastward-propagating beam of monthly periodic MRG waves. Figure 3b presents new evidence for this with a map of the mean eddy kinetic energy (EKE) near 1000 m, determined from the meridional velocity component v estimated from Argo float displacements (see Ollitrault and Colin de Verdière 2014); because near-equatorial v naturally peaks in the intraseasonal wave band, the plot indicates enhanced DEIV along the equator, especially in the eastern Pacific Ocean and western Atlantic Ocean where the TIW-generated MRG waves are expected (blue frames in Fig. 3b). Ascani et al. (2010) use surface forcing to generate an idealized beam of MRG waves in their numerical model. When the MRG waves are weak, a set of Eulerian mean currents resembling the EICs appear, but they are confined zonally within the beam and the associated Lagrangian mean currents are everywhere zero; when the MRG waves are strong, the EIC-like Eulerian mean currents are found within and to the west of the beam, extending to the western boundary, and they are associated with nonzero Lagrangian mean currents.[4]

The dynamical interpretation of these results given by Ascani et al. (2010) differs substantially from Hua et al.'s (2008) theory. Ascani et al. (2010) identified two types of wave instability. The first instability is the self-interaction of the MRG waves (a process neglected in Hua et al. 2008) that gives rise to EIC-like currents within the beam (but not outside). In the second instability, the MRG waves lose energy to other types of waves, especially small-vertical-scale ones where energy dissipation occurs. Unlike in Hua et al.'s (2008) scenario, the dissipation is key here because it alters potential vorticity at depth and enables the EIC-like currents resulting from the self-interaction to extend west of the beam, a process that is dynamically similar to the formation of a β-plume circulation (Stommel 1982; Pedlosky 1996; Kessler et al. 2003). Under this scenario, the EICs can be found over a very long zonal scale even if the MRG wave activity is itself zonally confined. We should also note that the focus differs between Hua et al. (2008) and Ascani et al. (2010); in the former, the focus is on the initial-value problem, while, in the latter, it is on the statistically steady-state problem. Despite these differences, however, both studies involve a transfer of energy from DEIV to EICs, and this is the fundamental property that we will check while studying the dynamics of EICs in our solutions (section 5b).

3. Experimental design

Our ocean model is a version of the Parallel Ocean Program (POP 2.0) model (e.g., Maltrud and McClean 2005), extending from 20°S to 20°N and from 58°W to

[4] Although the distinction between Eulerian and Lagrangian mean of the circulation is dynamically important (and central to understanding the effects of these currents on the distribution of tracers), the present work is concerned principally with the Eulerian mean. See Ascani et al. (2010) for a thorough discussion of the Lagrangian mean associated with the EICs.

TABLE 2. General characteristics of the configuration of each numerical solution. In each case, the wind stress is derived from observed winds over the Atlantic Ocean from the *ERS-1/2* scatterometer product. The realism of the configuration increases from top to bottom.

Name	Coastline	Wind stress
Solution 1	Rectangular	Time and zonally independent with a realistic meridional profile
Solution 1.5	Realistic	Time and zonally independent with a realistic meridional profile
Solution 1.8	Realistic	Time independent with a realistic zonal and meridional profile
Solution 2	Realistic	Varies climatologically, zonally, and meridionally

14°E to approximate the width of the equatorial Atlantic Ocean, with a flat bottom at 5000 m. Its horizontal resolution is ¼° in both longitude and latitude, and it has 100 levels, with the vertical resolution progressively decreasing from 10 m near the surface to 100 m near the bottom. Horizontal mixing is parameterized by biharmonic viscosity and diffusion with a coefficient of $-2 \times 10^{10}\,\mathrm{m^4\,s^{-1}}$, and vertical mixing follows the Richardson number–dependent scheme of Pacanowski and Philander (1981) with a background diffusivity of $10^{-5}\,\mathrm{m^2\,s^{-1}}$. We use a free-slip bottom boundary condition because preliminary experiments showed that quadratic bottom drag with a nondimensional drag coefficient of 1.225×10^{-3} reduces the DEIV barotropic energy by more than half, thereby significantly reducing the energy source for DEC (see section 6c).

We obtain four solutions (Table 2). The first (solution 1) is obtained in the rectangular basin noted above. It is forced over the whole domain by the zonal- and time-averaged winds observed over the Atlantic Ocean from the European Remote Sensing Satellite (*ERS-1/2*) scatterometer product; hence, the wind stress does not vary in longitude and time but has a realistic meridional profile. The second (solution 2) has the same configuration as solution 1, except that it is configured with a realistic coastline of the equatorial Atlantic Ocean (but still with vertical walls at the boundaries), and it is forced by the zonally, meridionally, and monthly varying *ERS-1/2* wind stress climatology. The first intermediate solution (solution 1.5) is similar to solution 1, except that it has a realistic coastline. The second intermediate solution (solution 1.8) differs from solution 2 only in having annual-mean winds (no annual cycle).

Sponge layers were not used in these simulations. Experiments including sponge layers on the northern and southern boundaries, implemented via Rayleigh damping, yielded EDJ basin modes but reduced their amplitude by half. This was apparently an indirect effect via reduction of the DEIV because in the simulations without sponge layers the high vertical mode coastal Kelvin wave energy does not reach the zonal boundaries, so it would be unaffected by sponge layers there.

The simulations are spun up from a state of rest. Temperature is initially horizontally uniform with a vertical profile derived from the observed potential temperature-averaged zonally and meridionally within 5° of the equator in the Atlantic (*World Ocean Atlas 2001*; Conkright et al. 2002), and surface temperature is relaxed to the climatological mean with a time scale of 1 month. Salinity is uniform at 35 throughout each simulation, a simplification that is acceptable for our purpose. The integrations span 50 yr for solution 1, 30 yr for solution 2, 9 yr for solution 1.5, and 15 yr for solution 1.8. The 5-day averages are archived in all years for solution 1 and in years 24–29 for solution 2. (The 5-day averages and snapshots are nearly identical.) The 1-yr means are archived for all years for solutions 1.5 and 1.8.

4. Model results

In this section, we report relevant aspects of the flow fields of solutions 1 and 2, describing first their upper-ocean circulation and DEIV (section 4a) and then their deep zonal currents that resemble the DEC (section 4b). We continue by presenting evidence that the spatial and temporal structure of the modeled EDJs in solution 1 matches that of quasi-resonant, low-frequency, baroclinic, equatorial basin modes (section 4c). We conclude with a brief description of the two intermediate solutions (solutions 1.5 and 1.8) to help to understand the differences between solutions 1 and 2.

a. Upper-ocean circulation and DEIV

Figure 5 shows the 5-yr mean, near-surface, zonal current and EKE from observations (top panels) and in solutions 1 and 2 (middle and bottom panels, respectively). The South Equatorial Current (SEC), the North Equatorial Countercurrent (NECC), and a fraction of the North Brazil Current (NBC) are well reproduced in solution 2 (Fig. 5e). In solution 1 (Fig. 5c), the NECC is about 50% stronger than observed mostly because the zonal width of the basin in solution 1 is larger than in the observations (see section 4d). The western boundary current is purely meridional, so there is no zonal component corresponding to the NBC.

The surface EKE field in solution 2 is overall more realistic than in solution 1. The high EKE region along the NECC in solution 2, however, is larger in amplitude

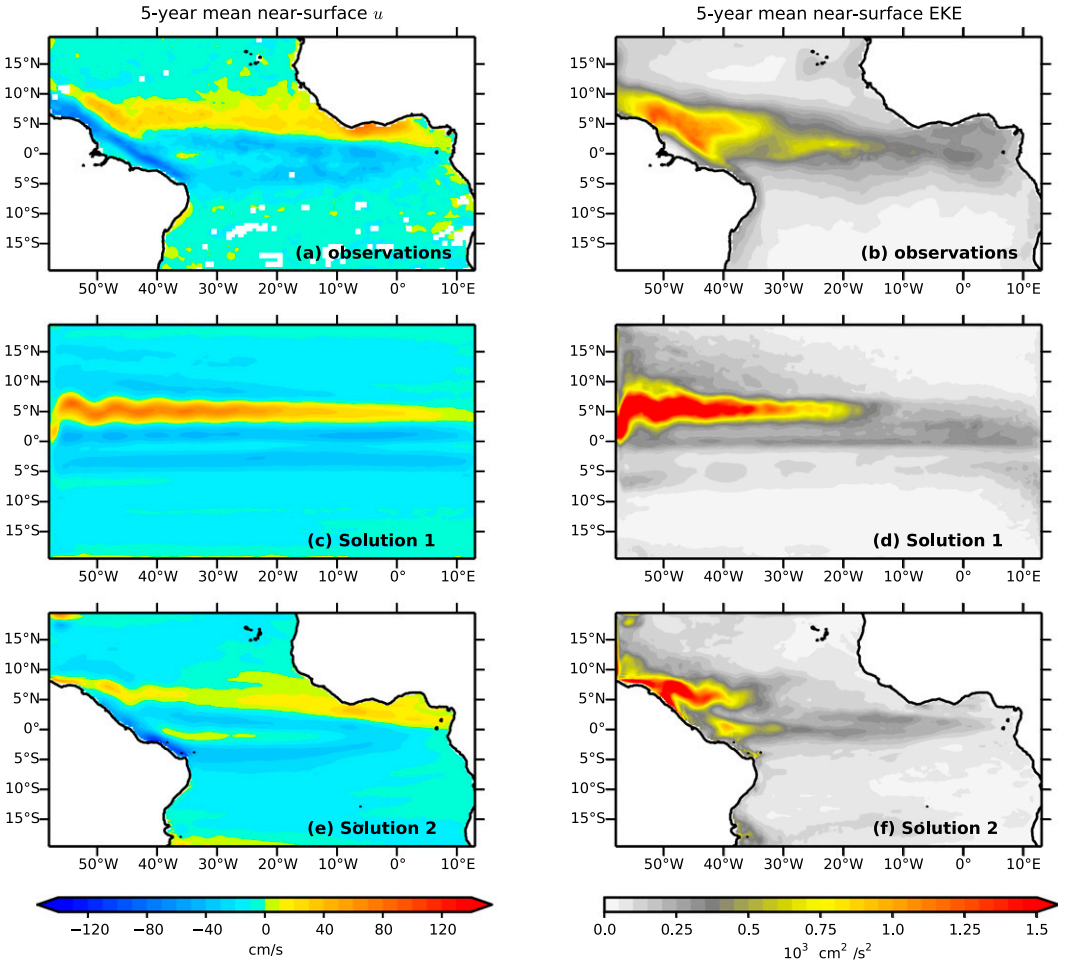

FIG. 5. 5-yr mean near-surface (left) u and (right) EKE in (top) the observations, (middle) solution 1, and (bottom) solution 2. Observations are from the Global Drifter Program (http://www.aoml.noaa.gov/phod/dac/dac_meanvel.php; Lumpkin and Johnson 2013). The velocity anomaly from the mean and seasonal cycle are used to construct EKE in both the observations and the simulations. Years 25 to 29 are used for the two runs. The black line corresponds to the coastline in the upper panels and to the 200-m isobath in the lower panels.

but smaller in zonal extent than in the observations. In solution 1, the high EKE region is stronger and more zonal than in the observations, but its zonal extent matches the observations.

The DEIV in solution 1 (Fig. 6) is similar to that in solution 2, but stronger in amplitude (Fig. 7). It is composed of large-vertical-scale Rossby waves with short periods (30–100 days), moderate meridional scale (~10°), and moderately short zonal wavelengths (5°–8°) (Figs. 6c,e). Near the equator, it includes MRG waves with a zonal wavelength of about 8° that are distributed over a range of vertical modes, with higher vertical modes corresponding to lower frequencies (Figs. 6d,f). The increase in small, vertical-scale energy at the equator is clearly visible in the time series of the meridional velocity component v at 5°N, 23°W and 0°, 23°W (Figs. 6a,b). Based on the analysis of a realistic simulation by von Schuckmann et al. (2008), we conclude that the large-vertical-scale waves of the DEIV correspond to the deep signature of TIWs and are forced by the instability of the upper-ocean circulation. With respect to the moderate to high vertical mode MRG waves at the equator, we will see in section 5c that they result instead from the formation mechanism that gives rise to the EDJs.

Spectra of v, zonally and vertically averaged along the equator (Fig. 7), are similar in shape for the two solutions but are weaker by a factor of about 3 in solution 2, consistent with the weaker, upper-ocean circulation in this run (Fig. 5). Using the velocity observations described by von Schuckmann et al. (2008), we compare observed and modeled equatorial v at 23°W using

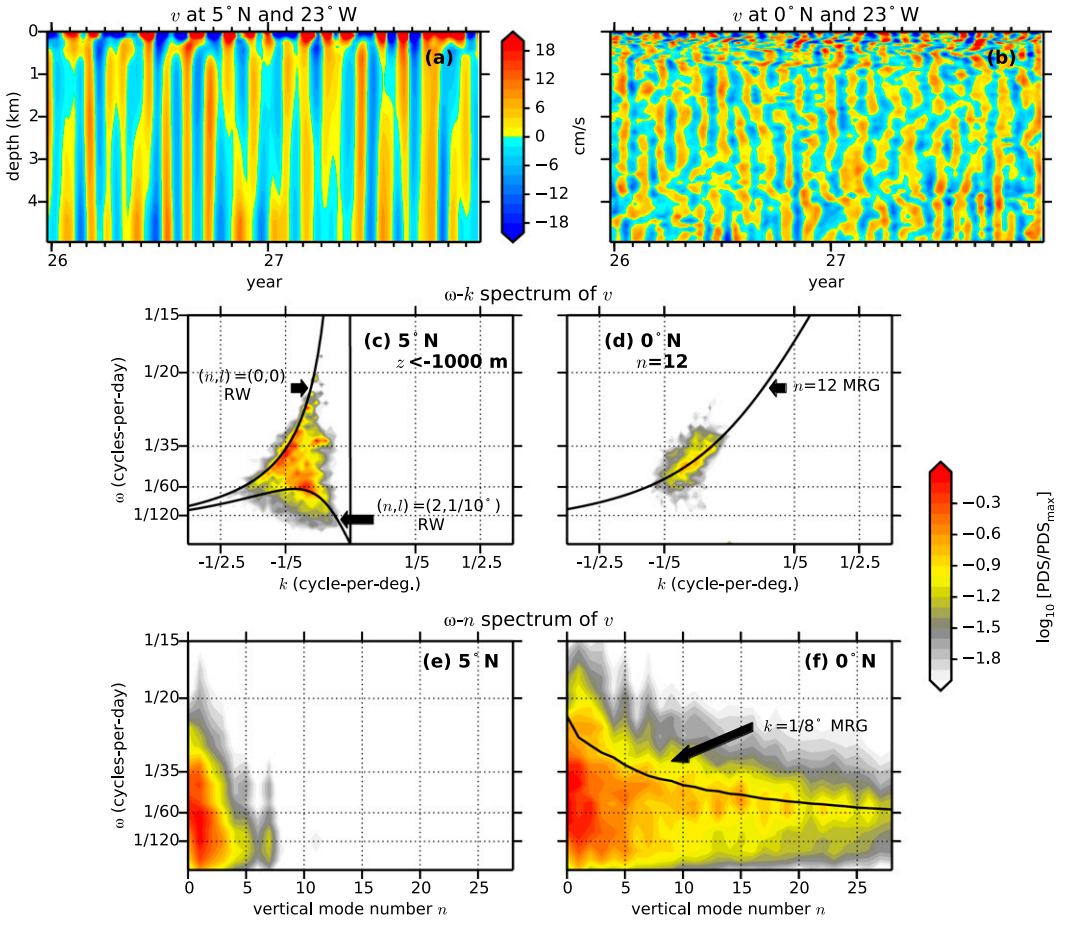

FIG. 6. Time series of the meridional component of velocity v at (a) (5°N, 23°W) and (b) (0°, 23°W) in solution 1. Frequency–horizontal wavenumber (ω–k) spectrum of v along (c) 5°N and (d) 0°. Frequency–vertical mode number (ω–n) spectrum of v along (e) 5°N and (f) 0°. Years 25 to 34 are used to construct all spectra. The ω–k spectrum in (c) is the average of spectra computed at every level below 1000-m depth, while the ω–k spectrum in (d) is the spectrum for the 12th baroclinic mode only. The ω–n spectrum is the average of spectra computed every 2° in longitude. All spectra are normalized by their maximum value before being plotted on a logarithmic scale. The black curves in (c) show the dispersion relations for the Rossby waves with $n = 0$ and zero meridional wavenumber ($l = 0$) and with $n = 2$ and $l =$ 1/10°. The black curve in (d) shows the dispersion relation for the $n = 12$ MRG wave, while the black curve in (f) shows the dispersion relation for all baroclinic MRG waves with a 8° zonal wavelength.

spectra calculated at every available depth between the surface and 700 m (Fig. 8). As already shown by von Schuckmann et al. (2008; their Fig. 3), there is an increase in DEIV for periods of 20–50 days between 100- and 300-m depth. A similar feature is seen in solution 2, and a more energetic version appears in solution 1. In both simulations, the DEIV energy elevation appears to extend deeper than in these observations. Model data comparisons of spectra of equatorial v are also performed using four additional datasets: the velocity measurements described by Bunge et al. (2008) at 23°W between 600- and 1500-m depth and at 10°W between 750- and 1700-m depth as well as the velocity observations collected during the World Ocean Circulation Experiment at 36°W between 3000- and 4000-m depth (mooring ACM10) and at 14.5°W between 1500- and 3000-m depth (mooring ACM11).[5] According to these comparisons, the intraseasonal meridional velocity in both simulations appears to be comparable to the observations above about 1500-m depth but is larger than in the observations by a factor of 3–4 below that depth (Fig. 9). Error bars are large, however, so it is not clear which solution reproduces a more realistic DEIV. Note also that both simulations lack energy at lower frequencies, especially at the two easternmost locations.

[5] Data along with references can be found at http://www.nodc.noaa.gov/woce/woce_v3/wocedata_1/cmdac/netcdf/explist.htm.

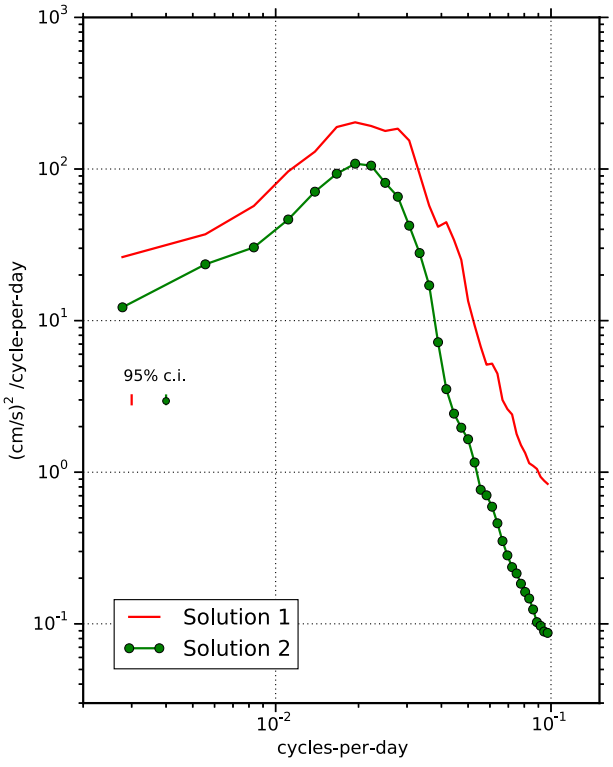

FIG. 7. Power density spectrum of equatorial v zonally and vertically averaged in solutions 1 and 2. The 1-yr-long time series from every 5° in longitude and 500 m in the vertical (between 1000 and 5000 m) are considered independent and used to compute the averaged spectrum. Each is detrended and a Hanning window is applied to it before performing the Fourier decomposition. This results in 630 segments with 1680 degrees of freedom (dof) in both cases (years 24 to 28). The same qualitative result is obtained if we use 35°W instead of 23°W for solution 1; 35°W is the same distance from the western boundary at the equator in solution 1 as 23°W is in the ocean (Fig. 5). The 95% confidence intervals are shown with vertical bars and are computed as described in von Storch and Zwiers (1999).

The Argo-derived meridional velocity components near 1000 m (Fig. 10) provide an estimate of the horizontal distribution of DEIV energy along the equator. At this depth, solution 1 reproduces the increase in EKE all along the equator (within 3°–4°), although it appears to somewhat overestimate its magnitude. In solution 2, however, the increase in EKE along the equator is much weaker. Quantitative comparison to Argo is not yet possible, given the available sampling.

In conclusion, it is not clear which of the two solutions reproduces a more realistic DEIV; it might be that solution 2 is more realistic over the depth range where the DEIV is the largest (upper 300 m; Fig. 8) but less so below at intermediate depths where the DEC is generated. Furthermore, this comparison to observations is hampered by severe undersampling, so that it is restricted to localized comparisons of energy level.

b. *Deep zonal currents*

The 5-day averages, 6-month averages, and 5-yr averages of the zonal current along 34°W in the simulations are shown in Fig. 11. In both runs, the 5-yr mean circulation is dominated by a set of large-vertical-scale flows spanning the whole water column and alternating with latitude. The three flows nearest the equator resemble the EICs described in section 2. They are, however, much more realistic in solution 1 than in solution 2; in solution 1, they attain current speeds of 5–10 cm s^{-1} and extend over nearly 40° longitude in the western half of the basin (Fig. 12), consistent with the observations, while in solution 2 their amplitude is only half as great and they are much less zonally coherent.

The 6-month mean in both solutions has a set of small-vertical-scale currents at the equator (Fig. 11, middle panels). In solution 1, the set of equatorial currents resembles the observed EDJs, with an amplitude reaching 10 cm s^{-1}; the vertical wavelength is about 1000 m, compared to about 600 m in the Atlantic. Consistent with quasi-synoptic observations (Fig. 1), the EDJs in solution 1 appear also in 5-day averages with an amplitude reaching 20 cm s^{-1} (Fig. 11, left panels). In solution 2, however, the set of equatorial currents does not have a well-defined vertical wavelength, and its amplitude reaches only a few centimeters per second, even in 5-day averages; it is unclear whether this set should be considered as a reasonable, albeit weak, reproduction of the EDJs.

The modeled EDJs in solution 1 are the most realistic reported so far in the literature, varying in time and depth in a fashion remarkably similar to the observations at 0°, 23°W (Fig. 2b). Figure 13 provides a depth–time plot of the low-frequency, zonal velocity u at 23°W in solution 1 [the quantity is scaled and the vertical coordinate is stretched with a reference buoyancy frequency of 1 cycle per hour (cph); Gill 1982]. Like the observed EDJs, the phase propagates downward and their energy upward, with a period of several years. Although both downward and upward energy propagation occurs within the first 12 yr of the run (not shown), the rest of the simulation is dominated by upward energy propagation, with a modulation at the decadal time scale (Fig. 13).

c. *Basin modes*

In agreement with the observations, the EDJs in solution 1 have properties consistent with their being the equatorial expressions of quasi-resonant, low-frequency, baroclinic, equatorial basin modes (section 2). The frequency–vertical wavenumber spectrum (Fig. 14) shows that zonal kinetic energy at the equator is

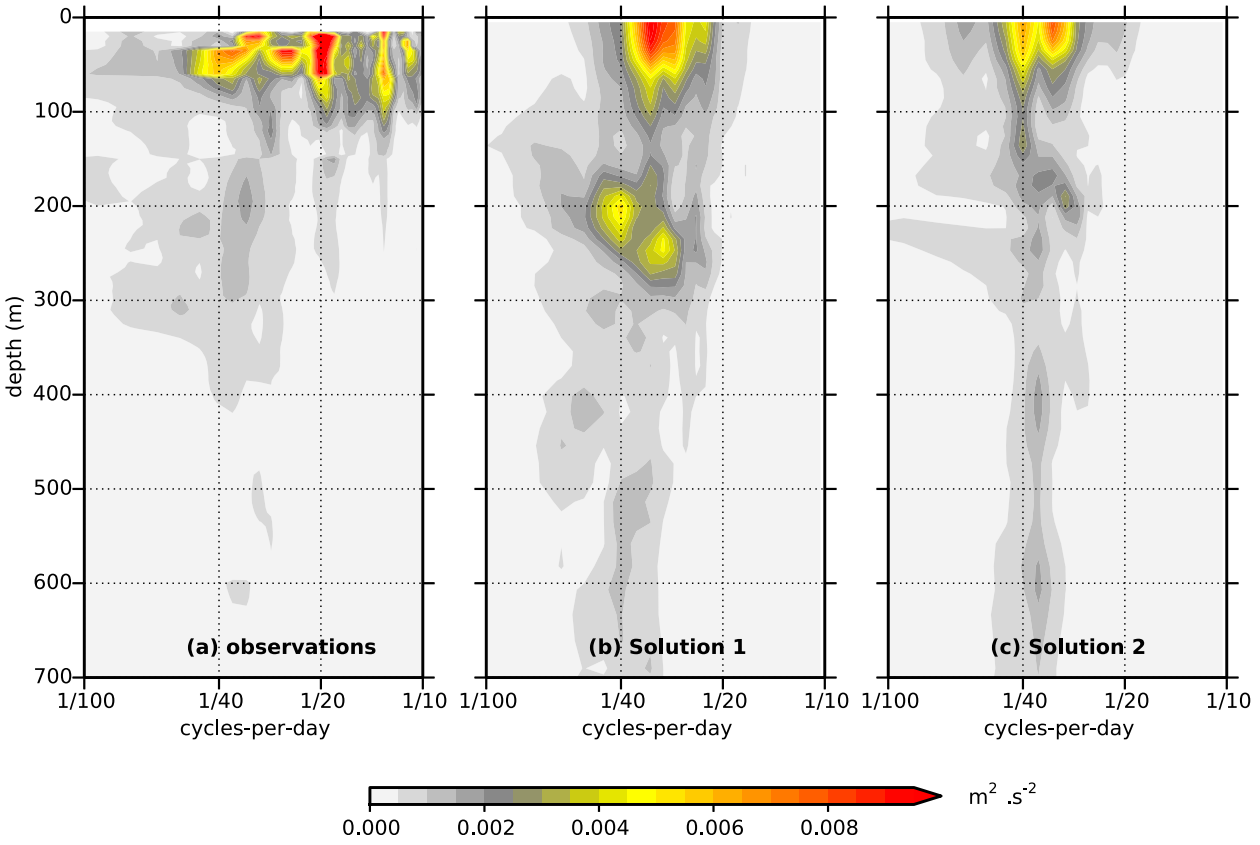

FIG. 8. Variance-preserving power density spectra of equatorial v at 23°W in (a) observations, (b) solution 1, and (c) solution 2. Spectral calculations are identical to those of Fig. 7 except that they are performed at every available depth and only at 23°W. This results in 5.4 segments on average for each depth (dof = 14) for the observations, 8 segments per depth (dof = 21; years 24 to 31) for solution 1, and 6 segments per depth (dof = 16; years 24 to 30) for solution 2. The observations are those reported in Brandt et al. (2012; 10-yr-long coverage).

concentrated near the basin mode prediction (1), with a preponderance of upward energy propagation. The lack of symmetry between downward and upward energy propagation suggests that the modes are energized at depth and dissipated nearer the thermocline; the upward-going energy decays to low values before reaching 300 m, and there is little or no energy descending from the 300-m level (Fig. 13). The energy of the basin modes is centered around vertical mode 12 and spans vertical modes 6 to 17. The observed Atlantic EDJs have their energy centered on vertical mode 15 and spread over vertical modes 12 to 20 (Brandt et al. 2008) so that the modeled EDJs in the run with idealized forcing correspond to somewhat larger vertical scales and shorter periods.

The spatiotemporal structure of the low-frequency u and pressure fields in solution 1 resembles that of basin modes. The similarity is illustrated in Fig. 15, which presents maps of u associated with upward-propagating energy for the stretched vertical wavelength of 930 m (vertical mode 12) with a resonant period of 3.9 yr. To fit the analytical solution from the theory of Cane and Moore (1981) to the numerical one, we used a Rayleigh damping coefficient $r(l) = |l|r_o$, where $r_o = 2 \times 10^{-9}\,\mathrm{s}^{-1}$, which increases linearly with the absolute meridional mode number $|l|$ to mimic the scale-dependent, biharmonic dissipation used in the numerical model.[6] We calculate the solution by summing over all odd meridional mode numbers between −1 and 51; this is a sufficient number of modes as about 90% of the variance is

[6] Although Rayleigh damping is not directly comparable to the Laplacian dissipation used in Greatbatch et al. (2012) to fit a numerical solution of the EDJ-like basin modes to observations, the magnitude of the damping used here appears somewhat weaker. Using Greatbatch et al.'s (2012) notation, if we assume that dissipation in their model is controlled by $A\partial_{yy}$, then r is equivalent to A/L_y^2 where L_y is a meridional scale. With $A = 300\,\mathrm{m}^2\,\mathrm{s}^{-1}$ and $Ly = 100\,\mathrm{km}$, A/L_y^2 is $3.10^{-8}\,\mathrm{s}^{-1}$. This discrepancy can be explained in part by the region and the criterion chosen for fitting; here, we use three longitudes and compare the shape of their y–t patterns, while in Greatbatch et al. (2012) the region between 30° and 15°W is used, and the fitting is based on the meridional width of the EDJs.

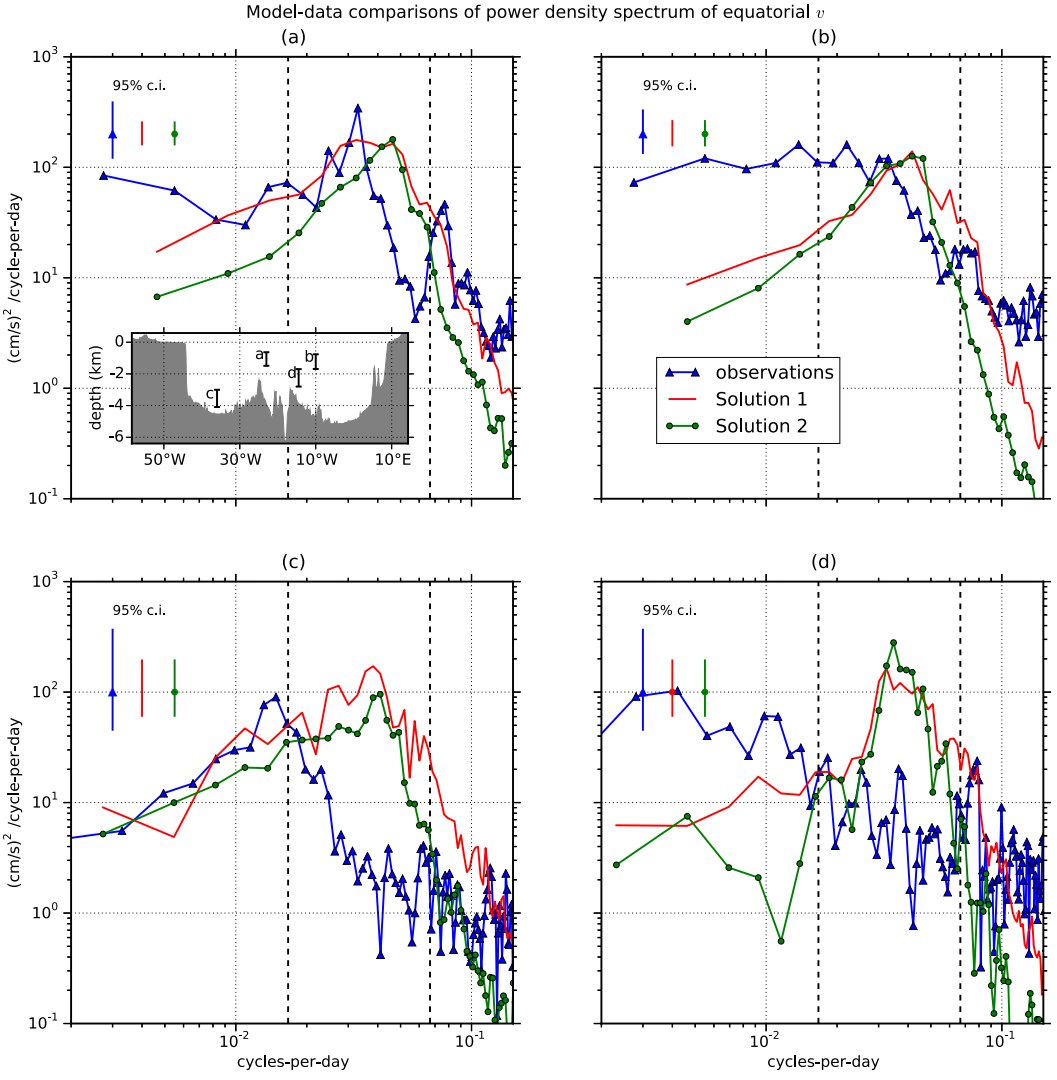

FIG. 9. Model data comparisons of power density spectrum of equatorial v: observations (blue), solution 1 (red), and solution 2 (green). Spectral calculations are conducted as for the spectra of Fig. 7 except that to construct the model spectra, we average spectra from the depths and locations that are near the actual moorings and either 1-yr or 20-month-long segments, depending on the duration of the data: (a) observations at 23°W described in Bunge et al. (2008), a total of nine 1-yr-long segments (dof = 32) from seven depths between 635- and 1486-m depth; (b) observations at 10°W also described in Bunge et al. (2008), a total of fifteen 1-yr-long segments (dof = 40) from nine depths between 764- and 1689-m depth; (c) observations from the ACM10 mooring, a total of three 20-month-long segments (dof = 8) at 3-, 3.6-, and 4.1-km depth; and (d) observations from the ACM11 mooring, a total of three 1-yr-long segments (dof = 8) at 1.7-, 2-, and 2.8-km depth. The longitude and depth range of each dataset is shown in the inlet panel in (a). Vertical dashed lines delimit the intraseasonal wave band (15–60-day period).

explained solely by the sum of the Kelvin wave ($l = -1$) and first meridional mode Rossby wave ($l = 1$). Differences between the numerical and analytical solution occur mainly at 20°W; at this longitude, the meridional width of the pattern is smaller in the analytical solution than in the numerical one, and there are phase differences between the two solutions on and off the equator. Despite these differences, the comparison in Fig. 15 supports the interpretation of the EDJs in solution 1 as being the sum of low-frequency baroclinic equatorial basin modes.[7]

In solution 2, the zonal motion along the equator is dominated by annual and semiannual waves with low

[7] Consistent with this conclusion, we have also checked that little energy is cycling back to the western boundary via Kelvin waves along the northern and southern boundaries.

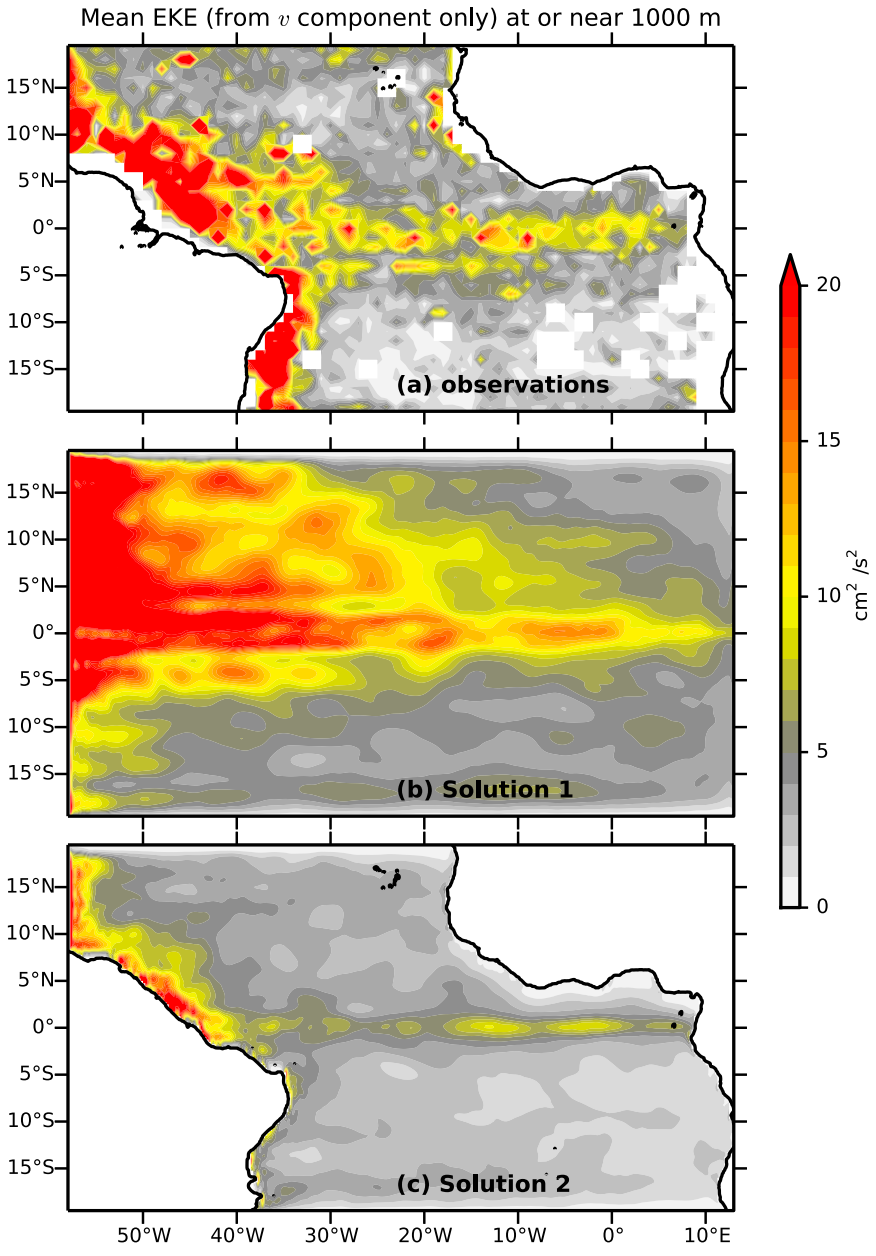

FIG. 10. Mean EKE near 1000-m depth from the v component only [i.e., $1/2\langle(v-\langle v\rangle)^2\rangle$, where the angle brackets indicate the time average]: (a) from Argo data as in Fig. 3b, (b) in solution 1, and (c) in solution 2. Average is over 1997–2014 for (a), and years 25 to 29 for (b) and (c). The model data have been low-pass filtered using a 10-day running mean before calculating the mean EKE in order to mimic the typical sampling scheme of the Argo data (about once every 10 days).

vertical wavenumbers and with net downward propagation of energy (Fig. 14b). The annual peaks occur at wavenumbers consistent with basin modes, as seen in previous numerical studies (Thierry et al. 2004). At lower frequencies, there is a weak local peak of upward-propagating energy that lies on the basin mode dispersion curve, with about the same moderately high vertical wavenumbers (0.9–1.2 $\times$ 10^{-3} cycles per meter) and frequencies ($\frac{1}{8}$–$\frac{1}{2}$ cycles per year) as in solution 1; however, the signal is no larger than other weak local peaks that are not on the basin mode curve, consistent with the lack of a clear EDJ signal in the time series of equatorial u of Fig. 2c or in the 6-month mean of Fig. 11e.

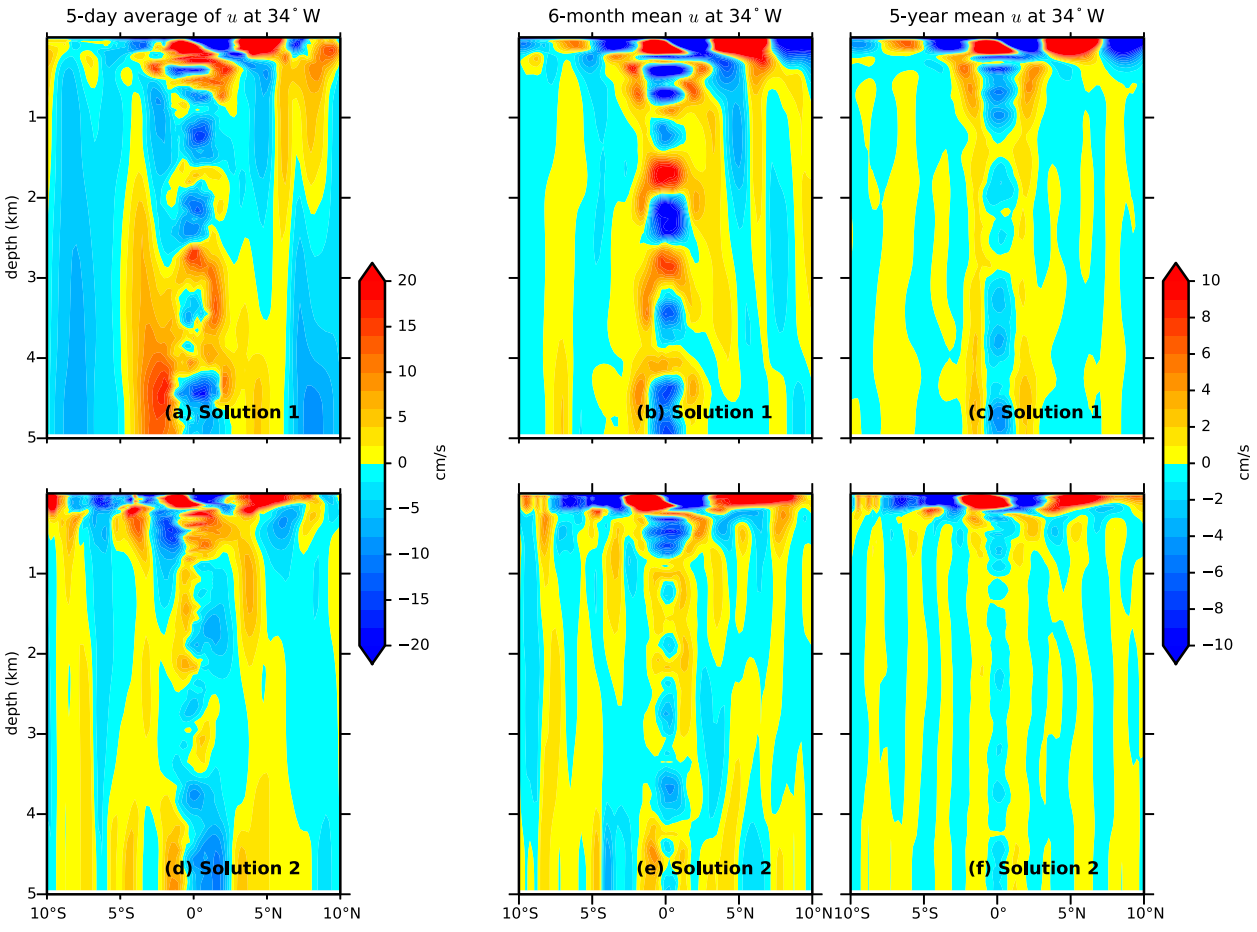

FIG. 11. (left) 5-day, (center) 6-month, and (right) 5-yr mean u at 34°W in (top) solution 1 and (bottom) solution 2. For both runs, the 5-day mean on 1 Jun of year 29, the second half of year 29, and years 25 to 29 are used for the 5-day mean, the 6-month mean, and the 5-yr mean, respectively. Notice the different color scale for the 5-day means and for the 6-month and 5-yr means.

d. Intermediate solutions

Finally, we conclude with a brief description of the two intermediate solutions 1.5 and 1.8. Both are closer to solution 2 than to solution 1, indicating that the differences between solution 1 and 2 are mostly because of the change in coastline rather a change in wind stress.

The upper-ocean circulation in solutions 1.5 and 1.8 is similar to that in solution 2 (not shown). In particular, the maximum speeds of the upper-ocean currents near the western boundary are reduced and reach the realistic level obtained in solution 2 once a realistic coastline is used. This is because the maximum amplitude of these currents is controlled mostly by the Sverdrup balance and depends on the zonal length over which the wind stress curl is integrated; with a reduced basin in the zonal direction once the realistic coastline is introduced, the maximum speed of the circulation is reduced as well. Consequently, the upper-ocean circulation is less unstable in the two intermediate solutions compared to solution 1, and their DEIV has a magnitude similar to that in solution 2. The DEC in solutions 1.5 and 1.8 is also similar in shape and amplitude to the DEC in solution 2 (not shown). One noticeable difference between solutions 1.5, 1.8, and 2, however, is that the EICs become weaker and less spatially coherent going from solution 1.5 to solution 1.8 to solution 2 (not shown); this suggests that some aspect of the DEC is sensitive to the zonal structure and annual cycle of the wind stress.

5. Dynamical interpretation

In section 4, we discussed basic properties of solutions 1 and 2, among other things, noting that they contain high-frequency energy (DEIV) and low-frequency structure (DEC). Here, we study the formation mechanism of the most realistic DEC (solution 1). To do so, we develop an analysis of the zonal kinetic energy budget in the frequency and wavenumber domain, using a stretched vertical coordinate (section 5a). This

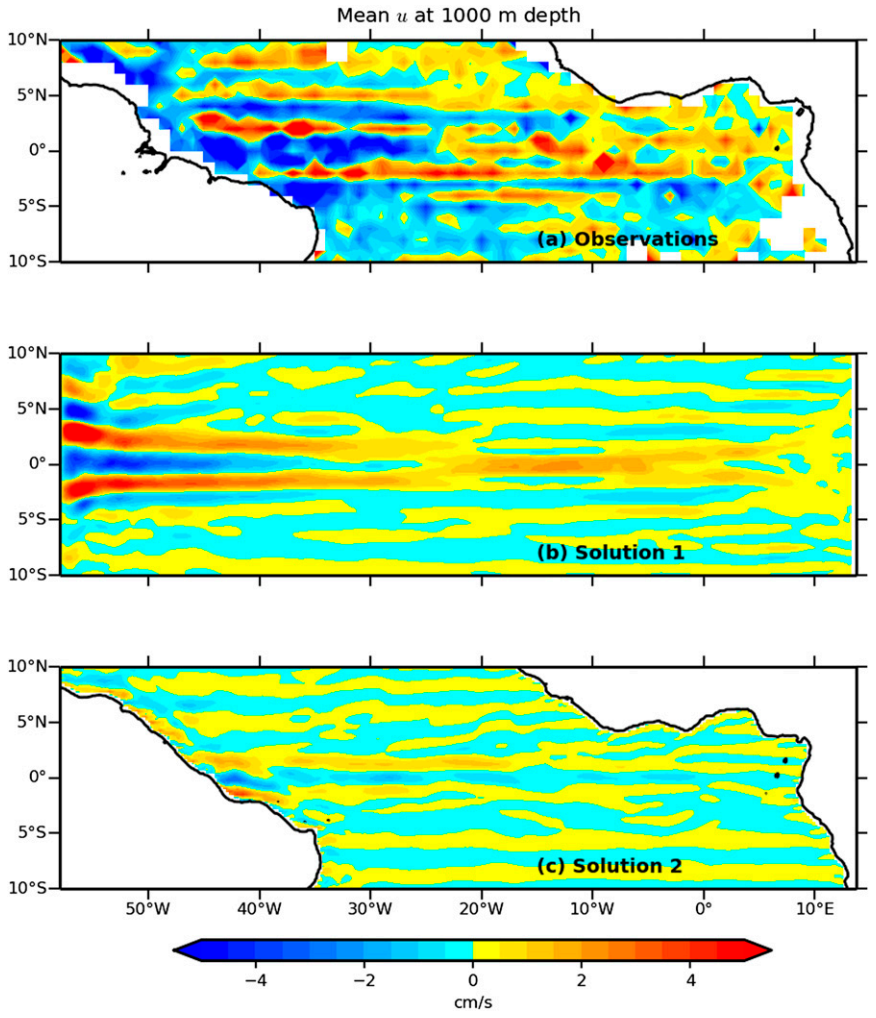

FIG. 12. Mean u at 1000 m (top) from Argo float displacements (see caption of Fig. 3) (middle) in solution 1 and (bottom) in solution 2. Years 25 to 29 are used for solution 1 and 2.

approach enables us to identify the set of nonlinear interactions among individual waves in the DEIV that produce the LEIC (section 5b) and EDJs (section 5c) in solution 1.[8]

a. *The zonal kinetic energy budget in frequency–vertical wavenumber space*

The zonal momentum equation at the equator is

$$u_t = -(uu_x + vu_y + wu_z) - \frac{1}{\rho_0}p_x + D_H^x + D_V^x, \quad (2)$$

where subscripts represent partial derivatives; u, v, and w are the zonal, meridional, and vertical components of the velocity field; p is pressure; ρ_0 is a constant reference density; and D_H^x and D_V^x are the zonal components of the horizontal and vertical viscous terms, respectively. Following Saltzman (1957), (2) is Fourier transformed in frequency–vertical wavenumber space:

$$i(2\pi f)\hat{u} = -(\widehat{uu_x} + \widehat{vu_y} + \widehat{wu_z}) - \frac{1}{\rho_0}\hat{p_x} + \widehat{D_H^x} + \widehat{D_V^x}, \quad (3)$$

where the hat represents the Fourier transform operator, and each quantity is a function of frequency f (in cycles per unit of time), wavenumber m in stretched vertical coordinate (in cycles per unit of stretched length), longitude x, and latitude y. We choose to represent the depth–time

[8] Although the Liouville–Green (also known as WKB) approximation used for scaling and stretching the dynamical quantities is not strictly valid for the large-vertical-scale MRG waves, it is used here simply as a rough-scale separation mechanism and does not affect our interpretation concerning the nonlinear interactions.

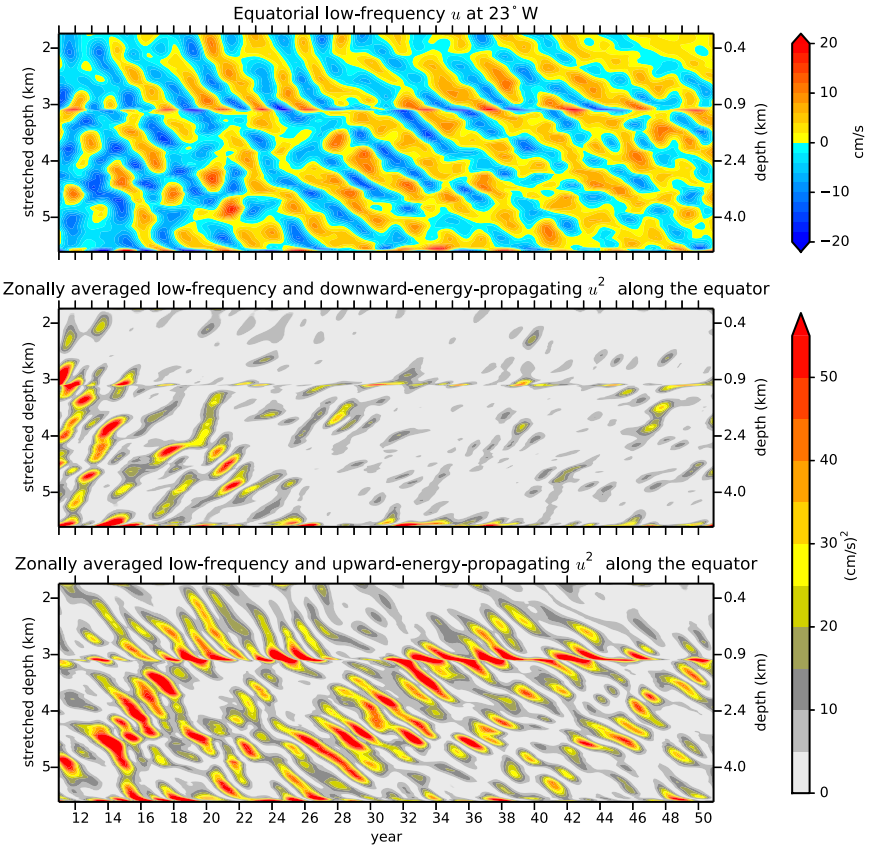

FIG. 13. (top) Time series of equatorial low-frequency (period > 1.75 yr) u at 23°W in solution 1. Velocity profiles below 300 m have been vertically stretched and scaled (using a reference buoyancy frequency of 1 cph; Gill 1982) before being plotted; the stretched and unstretched depth ticks are shown on the left and right axes, respectively. The squared amplitude averaged along the equator of the (middle) downward and (bottom) upward energy propagating u, respectively, are also plotted. The anomalously high values near 3100 stretched meters depth in these two panels result from unrealistically weak stratification in the reference profile at this depth.

dependence as $\exp[2\pi i(m_0 z + f_0 t)]$ so that $m_0 > 0$ and $f_0 > 0$ correspond to a downward phase and upward energy propagating signal. The zonal component of the kinetic energy equation in the frequency–vertical wavenumber space is thus

$$i(2\pi f)\hat{u}^*\hat{u} = -\hat{u}^*(\widehat{uu_x} + \widehat{vu_y} + \widehat{wu_z}) - \hat{u}^*\frac{1}{\rho_0}\widehat{p_x} + \hat{u}^*\widehat{D_H^x} + \hat{u}^*\widehat{D_V^x}, \quad (4)$$

where the asterisk denotes the complex conjugate. The left-hand side of (4) is imaginary, so the real parts of the terms on the right-hand side sum to zero with their relative magnitudes indicating how the "zonal" kinetic energy u^2 is generated and dissipated (Hayashi 1982). Calculating these terms for the equatorial slice below 300 m, we find a good numerical balance between the positive and negative contributions in (4) (Figs. 15a and 15b, respectively) for all frequencies and vertical wavenumbers. (A weak term $\hat{u}^*\widehat{D_H^x}$ is not shown.) Next, this energy balance is used to infer the relationships among the DEIV, LEIC, and EDJs.

b. Linkage of DEIV to LEIC

The LEIC is a time-mean flow with a large vertical scale, so it corresponds to the region of Fig. 16 near zero frequency and zero vertical wavenumber (small square in Fig. 16a). The two terms that perform positive work are the meridional and zonal advective terms ($-vu_y$ of Fig. 16a and $-uu_x$ of Fig. 16c, respectively), while the energy loss is mainly via the vertical advective term and zonal pressure gradient term ($-wu_z$ of Fig. 16d and $-p_x/\rho_0$ of Fig. 16e, respectively). To identify the nonlinear wave interactions that contribute to the maintenance of the LEIC against dissipation, we look at all pairs of waves (f_1, m_1) and (f_2, m_2) that contribute to the motion at $(f_0, m_0) = (0, 0)$ via the terms $-vu_y$ and $-uu_x$, where

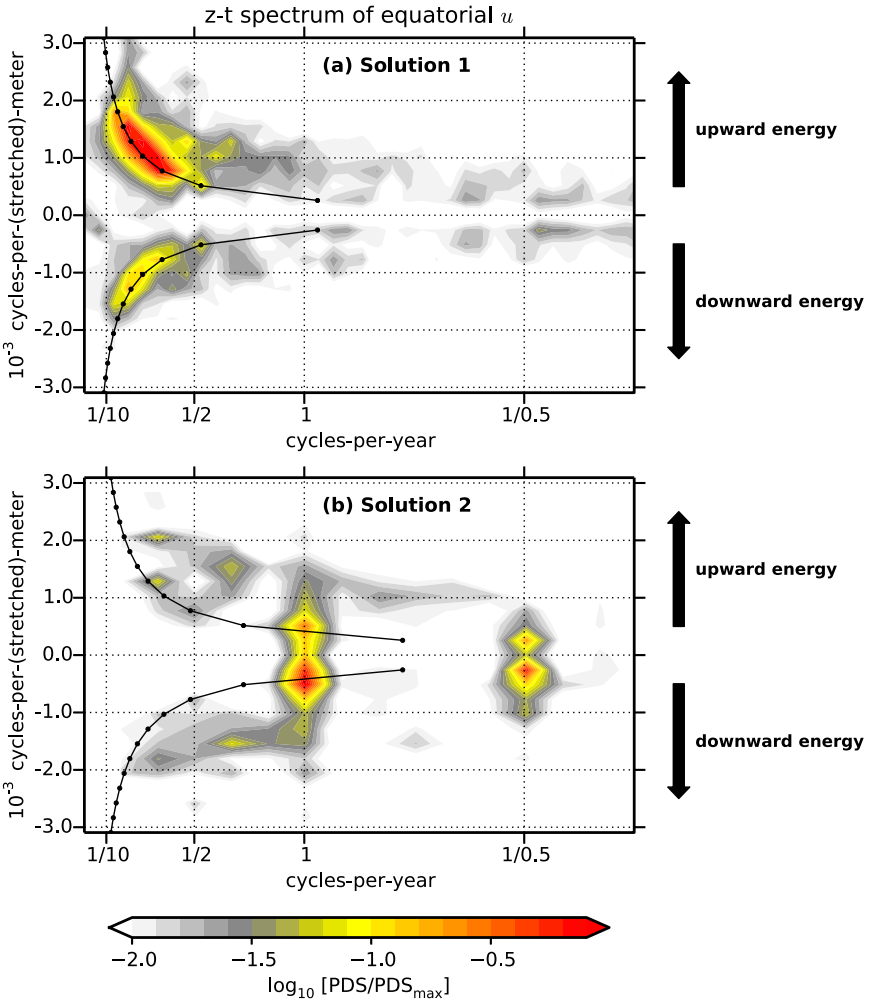

FIG. 14. Spectrum of equatorial u in the frequency–vertical wavenumber space: (a) solution 1 (years 10 to 49) and (b) solution 2 (years 24 to 29). Each spectrum is the average of spectra calculated every 2° along the equator and is normalized by its maximum value before being plotted on a logarithmic scale. For solution 1, the spectrum is computed from a set of 15-yr time series shifted in time every 2.5 yr; for solution 2, the full time series between years 24 and 29 is used. Velocity profiles below 300 m are stretched and scaled as in Fig. 13 before computing the spectra. The dotted black lines show the distribution of energy expected for low-frequency baroclinic equatorial basin modes [(1); Cane and Moore 1981].

$f_1 + f_2 = f_0$ and $m_1 + m_2 = m_0$. In the frequency–vertical wavenumber space that means we look at

$$-\hat{u}^*(f_0,m_0)\hat{v}(f_1,m_1)\widehat{u_y}(f_2,m_2) - \hat{u}^*(f_0,m_0)\hat{v}(f_2,m_2)\widehat{u_y}(f_1,m_1) \quad (5)$$

for $-vu_y$, and

$$-\hat{u}^*(f_0,m_0)\hat{u}(f_1,m_1)\widehat{u_x}(f_2,m_2) - \hat{u}^*(f_0,m_0)\hat{u}(f_2,m_2)\widehat{u_x}(f_1,m_1) \quad (6)$$

for $-uu_x$. Note that, for each expression, the first term is symmetric to the second one with respect to rotation around the point $(f_0/2, m_0/2)$. For the LEIC, $(f_0, m_0) = (0, 0)$, $f_1 = -f_2$, $m_1 = -m_2$, and the two terms in each expression are equal.

Quantities in (5) and (6) for $(f_0, m_0) = (0, 0)$ are plotted in Figs. 17 and 18, respectively. First, we find that the energy transfer via $-vu_y$ results from the interaction of high-frequency waves (mostly short Rossby waves with frequencies from 1/100 to 1/50 cycles per day) that are of large vertical scale (Fig. 17). This is consistent with the general mechanism proposed by Hua et al. (2008) and Ascani et al. (2010) that DEIV is one important source for the EICs via a transfer of energy from high-frequency

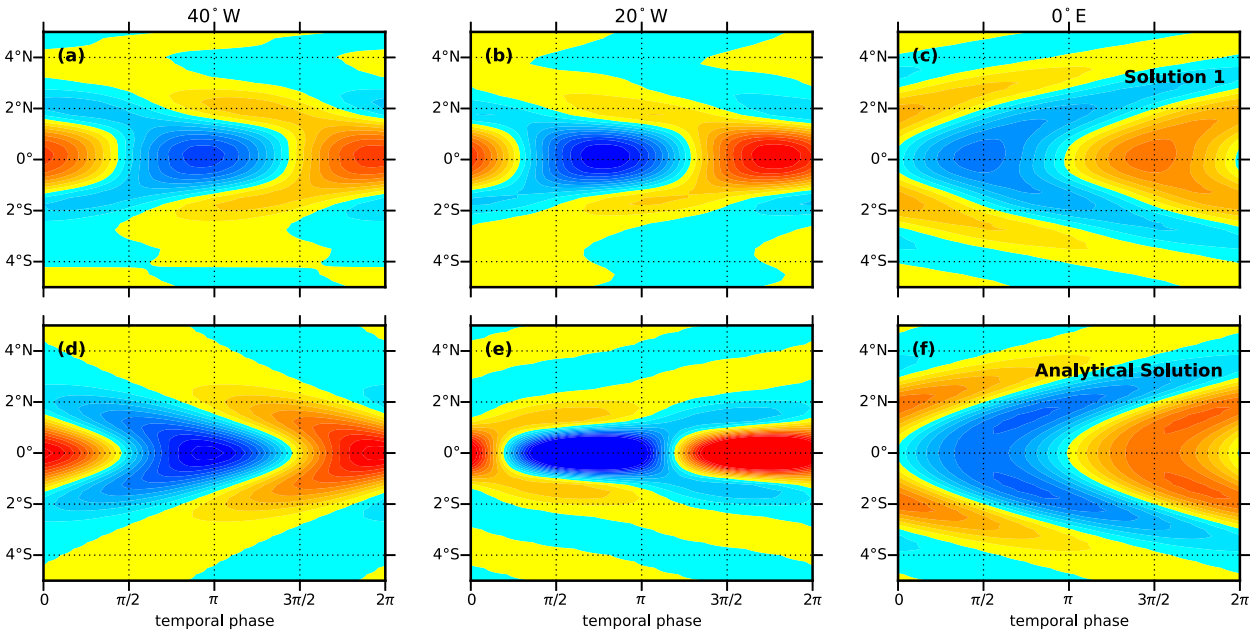

FIG. 15. Meridional and temporal structure of upward energy u at the 3.9-yr period and 930 stretched meters vertical wavelength (vertical mode 12) (top) from solution 1 and (bottom) from the theory of Cane and Moore (1981), with a Rayleigh damping coefficient $r = r_0[1, 2, \ldots, l]$ that is linearly increasing with the absolute meridional mode number $|l|$ with $r_0 = 2 \times 10^{-9}\,\mathrm{s}^{-1}$. The longitudes are (left) 40°W, (center) 20°W, and (right) 0°E. The abscissa is phase in radians over one period. The model and analytical solution have each been normalized by the maximum of its absolute value over the whole domain.

waves to the EICs.[9] Second, and quite unexpectedly, we also find an energy transfer from low-frequency baroclinic equatorial basin modes, corresponding to EDJs, to the LEIC via the $-uu_x$ term (Fig. 18); the interpretation is that each basin mode interacts with itself to transfer energy to the zero-frequency and zero vertical wavenumber component that corresponds to the LEIC. To check this result, we calculate the same work but in physical space, that is,

$$U^{\mathrm{EIC}}\langle -u^{\mathrm{EDJ}}u_x^{\mathrm{EDJ}}\rangle, \tag{7}$$

where U^{EIC} is the time-mean zonal velocity vertically averaged below 300 m, u^{EDJ} is the zonal velocity field associated with one particular basin mode (shown in Fig. 15), and the angle brackets indicate a time and vertical mean. In the western half of the basin, quantity (7) is positive at the equator and negative 2° on either side of it (Fig. 19), confirming that the EDJs tend to accelerate the LEIC (consistent with Fig. 18) and decelerate the NICC and SICC. This suggests that, in the statistically steady state, the transfer of energy that maintains the EICs is more complex than initially described by Hua et al. (2008) and Ascani et al. (2010) and involves not only a transfer from high- to low-frequency components but also between low-frequency components.

c. *Linkage of DEIV to EDJs*

All motions corresponding to the EDJs (dotted lines in Fig. 16) are maintained solely via the meridional advective term $-vu_y$, while energy loss is via the zonal advective term, the zonal pressure gradient term, and the vertical friction term ($-uu_x$ of Fig. 16c, $-p_x/\rho_0$ of Fig. 16e, and D_V^x of Fig. 16f, respectively). As for the LEIC, we identify the pairs of waves that contribute to a specific basin mode (f_0, m_0) via the term $-vu_y$ using expression (5), but two additional steps are performed initially. In the first step, we distinguish between the eastward- (Kelvin wave) and westward-propagating (long Rossby wave) components of the basin mode. Hence, the contribution to the Kelvin wave component of the basin mode is

$$\begin{aligned} &-\hat{u}^*(f_0, m_0; E)\hat{v}(f_1, m_1)\widehat{u_y}(f_2, m_2) \\ &\quad - \hat{u}^*(f_0, m_0; E)\hat{v}(f_2, m_2)\widehat{u_y}(f_1, m_1), \end{aligned} \tag{8}$$

[9] Although in Ascani et al. (2010), the high-frequency waves involved in the transfer have a vertical wavelength (~1700 m) smaller than those involved here, the transfer is not dependent on this vertical scale as the self-interaction of a wave field of any vertical wavelength produces a large, vertical-scale mean flow.

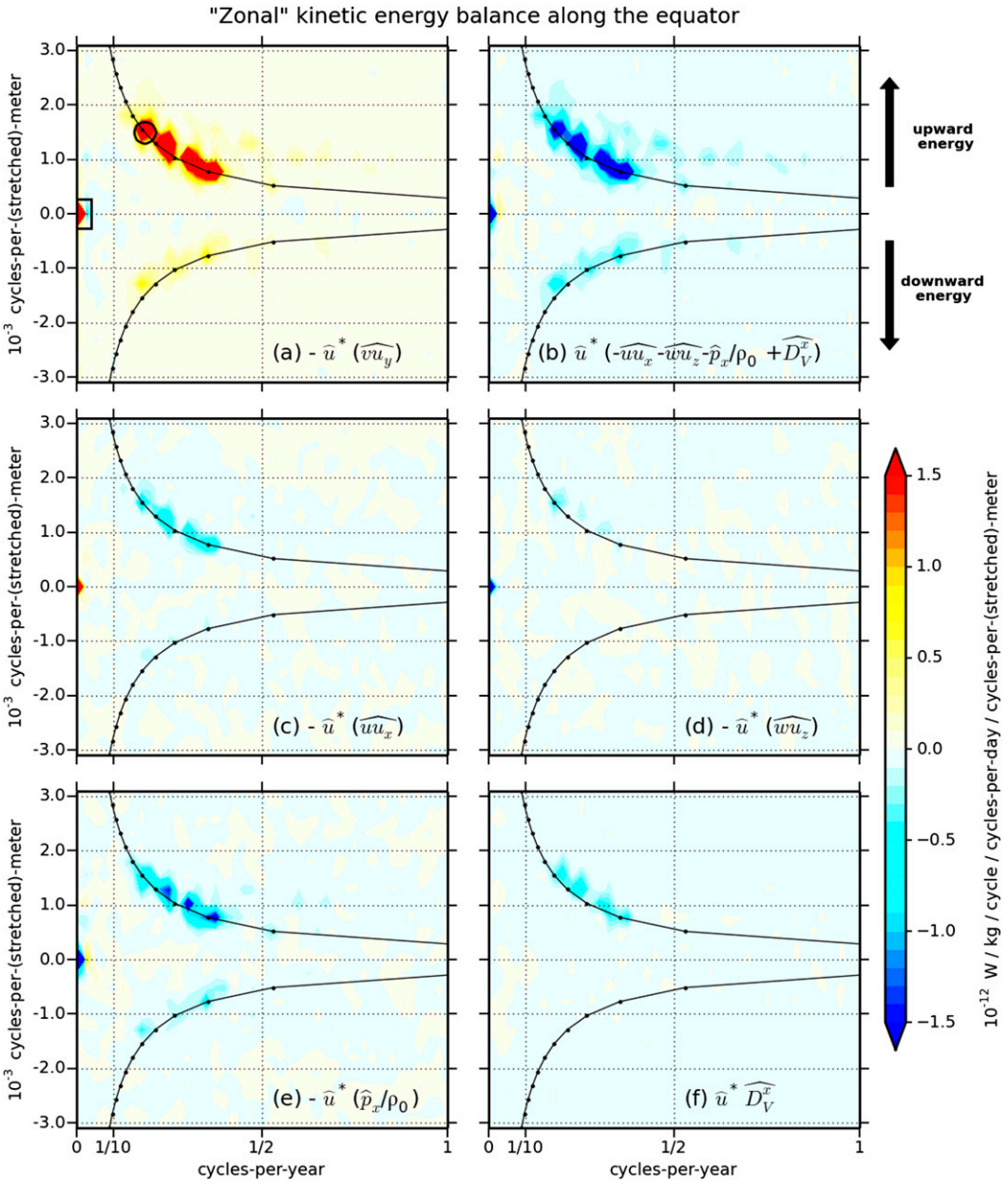

FIG. 16. Zonal kinetic energy budget: contribution to $\partial_t u^2$ in the frequency–vertical wavenumber space by the real part of (a) $-\hat{u}^*(\widehat{vu_y})$, (b) $\hat{u}^*(-\widehat{uu_x} - \widehat{wu_z} - \widehat{p_x}/\rho_0 + \widehat{D_V^x})$, (c) $-\hat{u}^*(\widehat{uu_x})$, (d) $-\hat{u}^*(\widehat{wu_z})$, (e) $-\hat{u}^*(\widehat{p_x}/\rho_0)$, and (f) $\hat{u}^*\widehat{D_V^x}$ along the equator in solution 1; see text for details. The term $\hat{u}^*\widehat{D_H^x}$ is weak and is not shown. Velocities from years 10 to 49 and below 300 m are stretched and scaled as in Fig. 13 before computing the spectra. The spectra are calculated every 2° in longitude and then averaged. The small box in (a) corresponds to the LEIC that is the focus of Figs. 17, 18, and 19, while the circle marks a basin mode that composes the EDJs and is the focus of Fig. 20. The dotted black lines show the basin mode dispersion relation as in Fig. 14.

and the contribution to the Rossby wave component of the basin mode is

$$-\hat{u}^*(f_0, m_0; W)\hat{v}(f_1, m_1)\widehat{u_y}(f_2, m_2) - \hat{u}^*(f_0, m_0; W)\hat{v}(f_2, m_2)\widehat{u_y}(f_1, m_1), \quad (9)$$

where $\hat{q}(f_i, m_i; E)$ and $\hat{q}(f_i, m_i; W)$ are the Fourier components of q at the frequency f_i and vertical wavenumber m_i with eastward (E) and westward (W) phase propagation, respectively. In the second step, we focus on wave pairs composed of waves with westward-propagating phase only; this reduces the noise in the

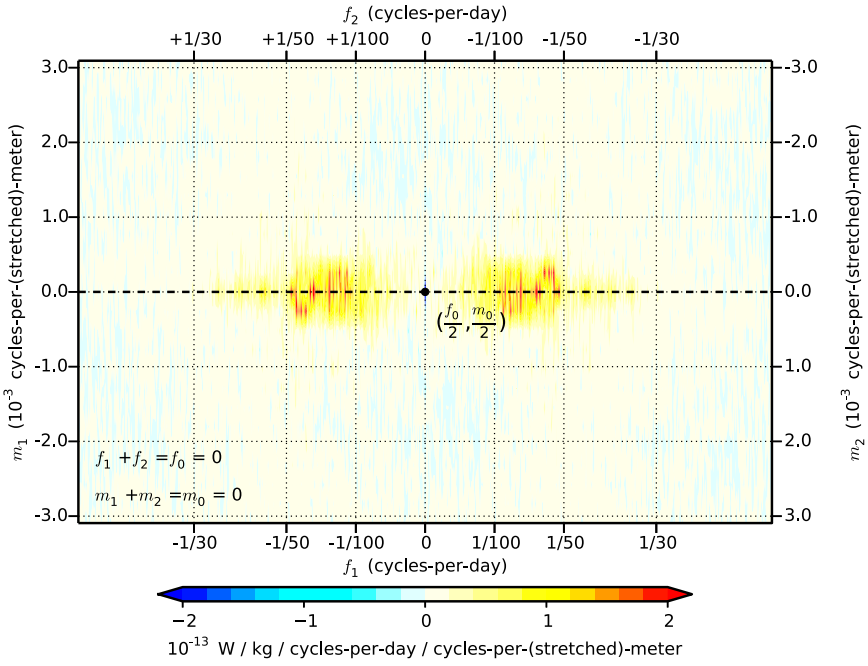

FIG. 17. Nonlinear energy transfer (in frequency–vertical wavenumber space) to the LEIC (f_0 = 0 and m_0 = 0; square symbol in Fig. 16a) via the term $-vu_y$ in solution 1 [(5)]. Positive values (red/yellow) indicate a transfer of energy to LEIC and the reverse for negative values (blue/cyan). The quantities (f_i, m_i) are the frequency and wavenumber (in stretched vertical coordinate) of the wave i = 1, 2. Spectra are calculated as in Fig. 16, but for 20-yr-long segments with 50% overlap, then averaged.

calculation without changing the pattern. Hence, quantities (8) and (9) become (10) and (11), respectively:

$$-\hat{u}^*(f_0,m_0;E)\hat{v}(f_1,m_1;W)\widehat{u_y}(f_2,m_2;W) - \hat{u}^*(f_0,m_0;E)\hat{v}(f_2,m_2;W)\widehat{u_x}(f_1,m_1;W), \quad (10)$$

and

$$-\hat{u}^*(f_0,m_0;W)\hat{v}(f_1,m_1;W)\widehat{u_y}(f_2,m_2;W) - \hat{u}^*(f_0,m_0;W)\hat{v}(f_2,m_2;W)\widehat{u_x}(f_1,m_1;W). \quad (11)$$

Quantities (10) and (11) are plotted in Fig. 20 for the (upward energy) basin mode with m_0 = 1/645 cycles per meter and the associated resonant frequency f_0 = 1/5.5 cycles per year (circle symbol in Fig. 16a); results are qualitatively similar for other upward energy basin modes. The plot demonstrates that the (f_0, m_0) motion is generated (red/yellow regions) from pairs of MRG waves that range in frequency from 1/100 to 1/30 cycles per day, with one wave having a low vertical wavenumber and the other having a vertical wavenumber close to m_0; these are the two types of high-frequency waves that were described in section 4a and Fig. 6. Note that the intraseasonal, high-vertical-wavenumber energy arises in situ as part of the interactions, while the low vertical wavenumber energy corresponds to TIWs and arises from remote instability of surface equatorial currents.[10] Further, the interactions between the two types of high-frequency waves contribute to both the Kelvin and Rossby wave components of the basin mode, with the interaction for the latter being somewhat stronger.

The aforementioned properties are generally consistent with the theory of Hua et al. (2008) for the EDJs. One difference, however, is that Hua et al. (2008) found that a MRG wave with a specific period gives rise to the EDJs at a specific vertical wavenumber, whereas in our solution, all MRG waves (from 30- to 100-day period) participate in the generation of any specified vertical mode. Another is that in Hua et al. (2008), MRG destabilization only generates the Kelvin wave component of high vertical mode basin modes, whereas we find that here it energizes both the Kelvin and long Rossby wave components. Hence, as for EICs, the nonlinear transfer of energy toward EDJs in the statistically steady state appears to be more complex than the transfer described in the initial-value problem studied by Hua et al. (2008).

[10] In the ocean, intraseasonal, high-vertical-wavenumber energy also arises directly from the instability of the surface equatorial currents (e.g., von Schuckmann et al. 2008), but this is somewhat underestimated in our model.

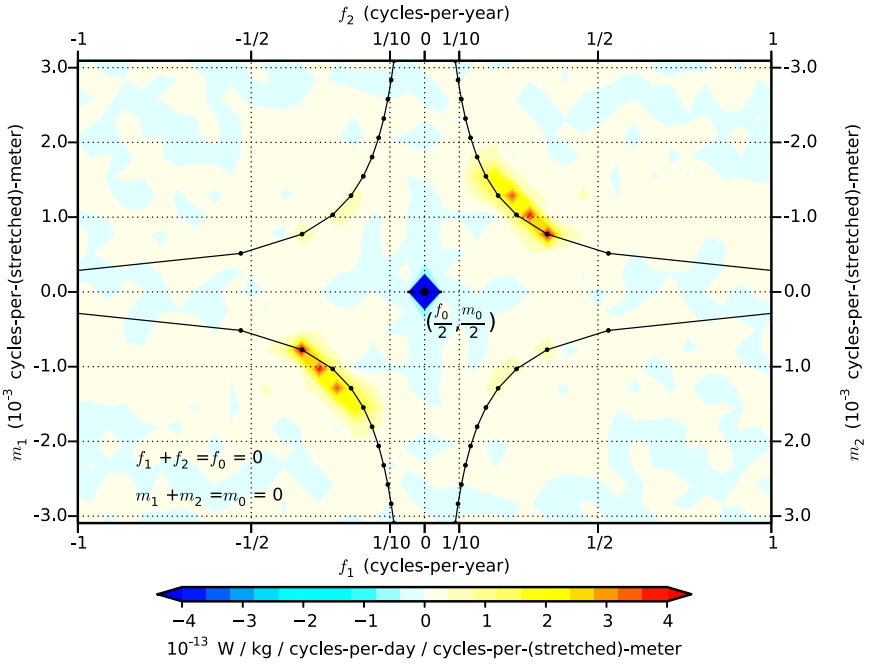

FIG. 18. As in Fig. 17, but for the term $-uu_x$ in solution 1 [(6)].

To address the issue of the asymmetry between upward and downward energy basin modes, we repeated the above analysis but for a downward energy basin mode. Quantities (10) and (11) are found weaker by an order of magnitude than in the upward energy case over all frequencies and vertical wavenumbers (not shown). This likely results from the weakness of the downward energy basin mode itself and unfortunately does not provide an explanation of why this is the case.

Finally, and for completeness, we also looked at the pair of waves that contribute to the dissipation of the (upward energy) EDJs via the term $-uu_x$. In contrast with the LEIC case, however, we found no pattern in the frequency–vertical wavenumber space (not shown).

6. Conclusions

a. Summary

The present study is an attempt to reproduce the DEC in a more realistic setting than in previous studies. In particular, instead of directly exciting a particular set of intraseasonal waves, the approach followed here is to let these waves arise from the instabilities of the large-scale circulation.

The DEC obtained in solution 1 (rectangular basin and steady wind forcing) has some realistic features. In particular, the EICs extend over a large zonal portion of the basin, while the EDJs form low-frequency quasi-resonant equatorial basin modes with energy propagating upward, consistent with the observations.

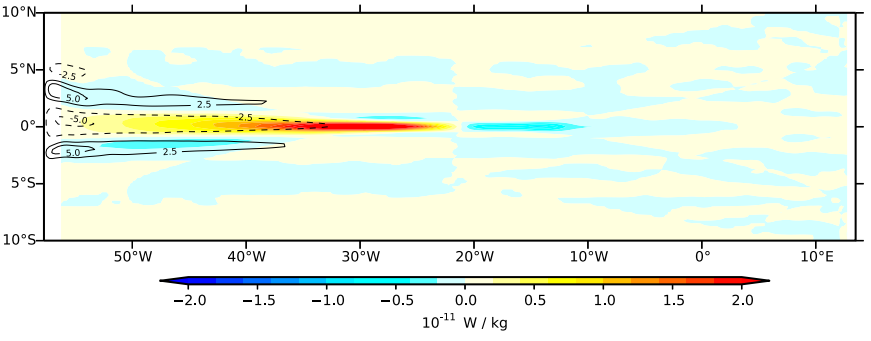

FIG. 19. Nonlinear energy transfer (in physical space) from a particular EDJ basin mode to EICs via the term $-uu_x$ [(7)]. The EDJs used in this calculation correspond to the theoretical basin mode shown in the lower panels of Fig. 15 with a maximum amplitude of 10 cm s^{-1}, while the EICs are defined as the time and vertical averaged zonal velocity below 300 m from solution 1 (years 25 to 29). Contours of EICs in centimeters per second are plotted in black.

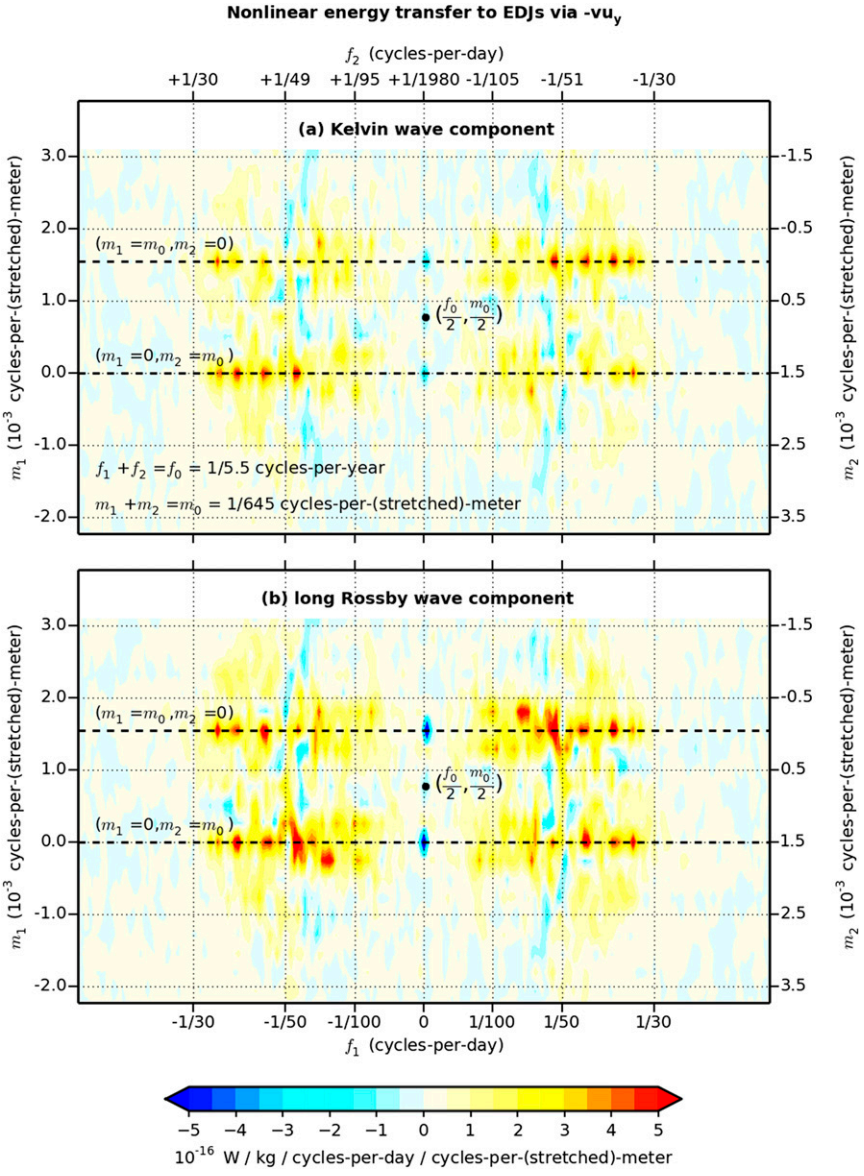

FIG. 20. Nonlinear transfer of energy (in frequency–vertical wavenumber space) to (a) the Kelvin wave component—[(10)]—and (b) long Rossby wave component—[(11)]—of a particular EDJ basin mode (f_0 = 1/5.5 cycles per year and m_0 = 1/645 cycles per meter; circle symbol in Fig. 16a) via the nonlinear term $-vu_y$ in solution 1. The meaning of the color code is the same as in Fig. 17. (f_i, m_i) are the frequency and wavenumber (in stretched vertical coordinate) of the wave i = 1, 2. Spectra are calculated as in Fig. 16, but for 5.5-yr-long segments with 50% overlap then averaged.

Further analyses of this simulation confirm the conclusion of previous studies that the DEC results from the rectification of DEIV. In particular, we show that the maintenance of both the EDJs and EICs is consistent with the instability and nonlinear modification of intraseasonal MRG and Rossby waves, as discussed by previous investigators (d'Orgeville et al. 2007; Hua et al. 2008; Ménesguen et al. 2009; Ascani et al. 2010). We still do not know, however, the cause for the energy difference between upward and downward energy EDJs. Finally, we find that EDJs contribute to the maintenance of the EICs, suggesting that the nonlinear transfer of energy in the statistically steady state is more complex than has been described previously.

A puzzling aspect of our study is that the DEC in solution 2, with more realistic coastlines and wind

forcing, is less realistic than in solution 1. Intermediate solutions 1.5 and 1.8 show that the primary factor is the reduction in basin width when coastlines are added. This reduces the speeds and instability of the upper-ocean currents, weakening the DEIV and hence leading to a weaker DEC.

b. *What can we conclude concerning the modeling of DEC?*

The DEC is the end result of a series of complex dynamical processes, some being nonlinear in nature. The mean upper-ocean circulation and deep western boundary currents near the equator give rise to instabilities that generate intraseasonal variability; some of that intraseasonal variability propagates away from its source as equatorial waves that then rectify into the mean and slowly varying DEC (Fig. 4). Hence, for a model to reproduce a realistic DEC, it needs to handle correctly each of these steps, any of which can be impaired by the model's deficiencies, such as a lack of spatial resolution, inadequate forcing, or unrealistic parameterization of subgrid-scale processes.

For the present solutions, the degree of realism of the DEC appears to depend critically on the amplitude and structure of the DEIV. Hence, we speculate that the model's limitations affect 1) the transfer of energy from the upper ocean to the DEIV and/or 2) the transfer of energy from the DEIV to the DEC.

Unfortunately, observations of the DEIV are inadequate for evaluating the DEIV in simulations. As concluded in section 4a, it is not clear which of our two solutions reproduces the more realistic DEIV. Although the DEIV in solution 1 may be too energetic over the depth range where it is the strongest (upper 300 m; Fig. 8), it may be more realistic than in solution 2 at intermediate depths, where the rectification into the DEC is most evident (Fig. 10). Indeed, there is one reason to believe that the deeper DEIV in solution 1 may be more realistic than in solution 2: von Schuckmann et al. (2008) noticed that the modeled DEIV energy can increase by a factor of 2 to 3 when using a daily rather than a climatological wind forcing. Hence, the unrealistically strong upper-ocean circulation and instabilities of solution 1 might compensate for the absence of intraseasonal and higher-frequency wind forcing and produce a more realistic deeper energy level for the DEIV compared to solution 2. Together with more observations of the DEIV, an additional simulation similar to solution 2 but with daily wind forcing would test this interpretation.

Alternatively, the DEIV might be closer to reality in solution 2 than in solution 1. In this case, the superior DEC representation in solution 1 might result from a cancellation of errors; perhaps deficiencies in the model's physics weaken the energy transfer from the DEIV to the DEC, and this is compensated by forcing an unrealistically strong DEIV. Indeed, there are three points supporting this interpretation. First, we know that in a model of a wide basin such as the Pacific, DEIV momentum dissipation is essential for the EICs to extend westward from their origin (Ascani et al. 2010), suggesting that it has to be well parameterized for EICs to have a realistic zonal extent. Second, the DEC is weak or nonexistent when horizontal Laplacian friction/diffusion and/or half the horizontal resolution (0.5° resolution) is used (not shown), suggesting again that the modeled DEC is sensitive to choices in spatial resolution and subgrid-scale parameterizations. Third, OGCMs have consistently underestimated the DEC, even when driven with current best estimates of the wind field and when performing quite well in simulating the upper-ocean circulation (Ascani 2005). Additional simulations to study the sensitivity of the energy transfer from DEIV to DEC to a model's resolution and parameters would be needed to confirm this interpretation.

c. *Effect of bottom friction*

During the course of performing these experiments, we found that a quadratic bottom drag with a nondimensional drag coefficient about half the typical value (1.225×10^{-3} vs 2.5×10^{-3}) damps dramatically both the DEIV and DEC (not shown). This is again consistent with the conclusion that DEIV is the source for the DEC in the simulations, and it may explain in part why the DEC is absent in some existing OGCMs. This hypothesis, however, is at odds with previous studies, showing that a moderately strong bottom friction is needed to reproduce a realistic level of EKE in OGCMs (Arbic et al. 2009).

d. *Additional issues*

Other issues have not been addressed in the present study. First, bottom topography is not included in any of our simulations; given that even simple parameterized bottom friction was found to reduce DEIV and DEC and was therefore omitted, we expect the roughness and blocking effects of the Mid-Atlantic Ridge must be important for the DEIV and DEC. Second, it is unclear whether the zonal jets found poleward of the EICs (e.g., Qiu et al. 2013) are dynamically similar to the EICs. Finally, we have not studied the Lagrangian transport associated with the time-varying DEC, which affects the zonal distribution of biogeochemical properties (Getzlaff and Dietze 2013; Dietze and Loeptien 2013). This transport is a function of the model dissipation (Ascani et al. 2010), and the analysis of the Lagrangian

component of the DEC as a function of subgrid-scale parameterization, in a model capable of simulating a realistic DEC, would be needed to address this important issue.

Acknowledgments. We dedicate this paper to the memory of Bach Lien Hua, who contributed so much to the understanding of the dynamics of the EDJs and EICs. We thank Dailin Wang who actively contributed to the first phase of this study and to Christine Provost and Lucia Bunge who kindly shared their velocity data with us. We also thank the two anonymous reviewers for their constructive comments. The surface drifter climatology of ocean currents has been developed by NOAA/AOML/PMEL and can be found online (at http://www.aoml.noaa.gov/phod/dac/dac_meanvel.php). The YoMaHa product is developed by the International Pacific Research Center (IPRC) at the University of Hawaii and is available online (at http://apdrc.soest.hawaii.edu/projects/Argo/index.php). This work was funded in part by NSF Grant OCE0327334 (FA and EF), the IPRC (FA), the German Science Foundation as part of the Sonderforschungsbereich 754 "Climate-Biogeochemistry Interactions in the Tropical Ocean," by the German Federal Ministry of Education and Research Grant 03F0651B and by European Union 7th Framework Programme (FP7 2007-2013) under Grant Agreement 603521 PREFACE (PB and RJG). PB and RJG are also grateful for continuing support from GEOMAR. Moored velocity observations at the equator were acquired in cooperation with the Prediction and Research Moored Array in the Tropical Atlantic (PIRATA) project.

REFERENCES

Arbic, B. K., and Coauthors, 2009: Estimates of bottom flows and bottom boundary layer dissipation of the oceanic general circulation from global high-resolution models. *J. Geophys. Res.,* **114,** C02024, doi:10.1029/2008JC005072.

Ascani, F., 2005: The equatorial subthermocline circulation in ocean general circulation models. M.S. thesis, Dept. of Oceanography, University of Hawai'i at Mānoa, 67 pp.

——, E. Firing, P. Dutrieux, J. P. McCreary, and A. Ishida, 2010: Deep equatorial ocean circulation induced by a forced-dissipated Yanai beam. *J. Phys. Oceanogr.,* **40,** 1118–1142, doi:10.1175/2010JPO4356.1.

Bourlès, B., M. d'Orgeville, G. Eldin, Y. Gouriou, R. Chuchla, Y. du Penhoat, and S. Arnault, 2002: On the evolution of the thermocline and subthermocline eastward currents in the equatorial Atlantic. *Geophys. Res. Lett.,* **29,** doi:10.1029/2002GL015098.

——, and Coauthors, 2003: The deep currents in the eastern equatorial Atlantic Ocean. *Geophys. Res. Lett.,* **30,** 8002, doi:10.1029/2002GL015095.

Brandt, P., V. Hormann, B. Bourles, J. Fischer, F. A. Schott, L. Stramma, and M. Dengler, 2008: Oxygen tongues and zonal currents in the equatorial Atlantic. *J. Geophys. Res.,* **113,** C04012, doi:10.1029/2007JC004435.

——, A. Funk, V. Hormann, M. Dengler, R. J. Greatbatch, and J. M. Toole, 2011: Interannual atmospheric variability forced by the deep equatorial Atlantic Ocean. *Nature,* **473,** 497–500, doi:10.1038/nature10013.

——, and Coauthors, 2012: Ventilation of the equatorial Atlantic by the equatorial deep jets. *J. Geophys. Res.,* **117,** C12015, doi:10.1029/2012JC008118.

Bunge, L., C. Provost, B. L. Hua, and A. Kartavtseff, 2008: Variability at intermediate depths at the equator in the Atlantic Ocean in 2000–06: Annual cycle, equatorial deep jets, and intraseasonal meridional velocity fluctuations. *J. Phys. Oceanogr.,* **38,** 1794–1806, doi:10.1175/2008JPO3781.1.

Cane, M. A., and D. W. Moore, 1981: A note on low-frequency equatorial basin modes. *J. Phys. Oceanogr.,* **11,** 1578–1584, doi:10.1175/1520-0485(1981)011<1578:ANOLFE>2.0.CO;2.

Conkright, M. E., R. A. Locarnini, H. E. Garcia, T. D. O'Brien, T. P. Boyer, C. Stephens, and J. I. Antonov, 2002: World Ocean Atlas 2001: Objective analysis, data statistics, and figures, CD-ROM documentation. National Oceanographic Data Center Internal Rep. 17, 17 pp. [Available online at http://odv.awi.de/fileadmin/user_upload/odv/data/WOA01/README.PDF.]

Cravatte, S., W. S. Kessler, and F. Marin, 2012: Intermediate zonal jets in the tropical Pacific Ocean observed by Argo floats. *J. Phys. Oceanogr.,* **42,** 1475–1485, doi:10.1175/JPO-D-11-0206.1.

Czeschel, R., L. Stramma, F. U. Schwarzkopf, B. S. Giese, A. Funk, and J. Karstensen, 2011: Middepth circulation of the eastern tropical South Pacific and its link to the oxygen minimum zone. *J. Geophys. Res.,* **116,** C01015, doi:10.1029/2010JC006565.

Dietze, H., and U. Loeptien, 2013: Revisiting "nutrient trapping" in global coupled biogeochemical ocean circulation models. *Global Biogeochem. Cycles,* **27,** 265–284, doi:10.1002/gbc.20029.

d'Orgeville, M., B. L. Hua, and H. Sasaki, 2007: Equatorial deep jets triggered by a large vertical scale variability within the western boundary layer. *J. Mar. Res.,* **65,** 1–25, doi:10.1357/002224007780388720.

Eden, C., 2006: Middepth equatorial tracer tongues in a model of the Atlantic Ocean. *J. Geophys. Res.,* **111,** C12025, doi:10.1029/2006JC003565.

——, and M. Dengler, 2008: Stacked jets in the deep equatorial Atlantic Ocean. *J. Geophys. Res.,* **113,** C04003, doi:10.1029/2007JC004298.

Firing, E., 1987: Deep zonal currents in the central equatorial Pacific. *J. Mar. Res.,* **45,** 791–812, doi:10.1357/002224087788327163.

——, S. Wijffels, and P. Hacker, 1998: Equatorial subthermocline currents across the Pacific. *J. Geophys. Res.,* **103,** 21 413–21 423, doi:10.1029/98JC01944.

Getzlaff, J., and H. Dietze, 2013: Effects of increased isopycnal diffusivity mimicking the unresolved equatorial intermediate current system in an Earth system climate model. *Geophys. Res. Lett.,* **40,** 2166–2170, doi:10.1002/grl.50419.

Gill, A. E., 1982: *Atmosphere–Ocean Dynamics.* Academic Press, 662 pp.

Gouriou, Y., B. Bourlès, H. Mercier, and R. Chuchla, 1999: Deep jets in the equatorial Atlantic Ocean. *J. Geophys. Res.,* **104,** 21 217–21 226, doi:10.1029/1999JC900057.

——, and Coauthors, 2001: Deep circulation in the equatorial Atlantic Ocean. *Geophys. Res. Lett.,* **28,** 819–822, doi:10.1029/2000GL012326.

Greatbatch, R. J., P. Brandt, M. Claus, S.-H. Didwischus, and Y. Fu, 2012: On the width of the equatorial deep jets. *J. Phys. Oceanogr.,* **42,** 1729–1740, doi:10.1175/JPO-D-11-0238.1.

Hayashi, Y., 1982: Interpretations of space-time spectral energy equations. *J. Atmos. Sci.,* **39,** 685–688, doi:10.1175/1520-0469(1982)039<0685:IOSTSE>2.0.CO;2.

Hua, B. L., M. d'Orgeville, M. D. Fruman, C. Ménesguen, R. Schopp, P. Klein, and H. Sasaki, 2008: Destabilization of mixed Rossby gravity waves and the formation of equatorial zonal jets. *J. Fluid Mech.,* **610,** 311–341, doi:10.1017/S0022112008002656.

Ishida, A., Y. Kashino, H. Mitsudera, N. Yosioka, and T. Kadokura, 1998: Preliminary results of a global high-resolution GCM experiment. *J. Fac. Sci. Hokkaido Univ.,* **11,** 441–460.

Johnson, G. C., and D. Zhang, 2003: Structure of the Atlantic Ocean equatorial deep jets. *J. Phys. Oceanogr.,* **33,** 600–609, doi:10.1175/1520-0485(2003)033<0600:SOTAOE>2.0.CO;2.

——, E. Kunze, K. E. McTaggart, and D. W. Moore, 2002: Temporal and spatial structure of the equatorial deep jets in the Pacific Ocean. *J. Phys. Oceanogr.,* **32,** 3396–3407, doi:10.1175/1520-0485(2002)032<3396:TASSOT>2.0.CO;2.

Kessler, W. S., G. C. Johnson, and D. W. Moore, 2003: Sverdrup and nonlinear dynamics of the Pacific equatorial currents. *J. Phys. Oceanogr.,* **33,** 994–1008, doi:10.1175/1520-0485(2003)033<0994:SANDOT>2.0.CO;2.

Lebedev, K. V., H. Yoshinari, N. A. Maximenko, and P. W. Hacker, 2007: YoMaHa'07: Velocity data assessed from trajectories of Argo floats at parking level and at the sea surface. IPRC Tech. Note 4, 16 pp.

Lumpkin, R., and G. C. Johnson, 2013: Global ocean surface velocities from drifters: Mean, variance, El Niño–Southern Oscillation response, and seasonal cycle. *J. Geophys. Res.,* **118,** 2992–3006, doi:10.1002/jgrc.20210.

Luyten, J. R., and F. C. Swallow, 1976: Equatorial undercurrents. *Deep-Sea Res. Oceanogr. Abstr.,* **23,** 999–1001, doi:10.1016/0011-7471(76)90830-5.

Maltrud, M. E., and J. L. McClean, 2005: An eddy resolving global 1/10° ocean simulation. *Ocean Modell.,* **8,** 31–54, doi:10.1016/j.ocemod.2003.12.001.

Ménesguen, C., B. L. Hua, M. D. Fruman, and R. Schopp, 2009: Dynamics of the combined extra-equatorial and equatorial deep jets in the Atlantic. *J. Mar. Res.,* **67,** 323–346, doi:10.1357/002224009789954766.

Ollitrault, M., and A. Colin de Verdière, 2014: The ocean general circulation near 1000-m depth. *J. Phys. Oceanogr.,* **44,** 384–409, doi:10.1175/JPO-D-13-030.1.

——, M. Lankhorst, D. Fratantoni, P. Richardson, and W. Zenk, 2006: Zonal intermediate currents in the equatorial Atlantic Ocean. *Geophys. Res. Lett.,* **33,** L05605, doi:10.1029/2005GL025368.

Pacanowski, R., and S. Philander, 1981: Parametrization of vertical mixing in numerical models of tropical oceans. *J. Phys. Oceanogr.,* **11,** 1443–1451, doi:10.1175/1520-0485(1981)011<1443:POVMIN>2.0.CO;2.

Pedlosky, J., 1996: *Ocean Circulation Theory.* Springer-Verlag, 453 pp.

Qiu, B., S. Chen, and H. Sasaki, 2013: Generation of the North Equatorial Undercurrent jets by triad baroclinic Rossby wave interactions. *J. Phys. Oceanogr.,* **43,** 2682–2698, doi:10.1175/JPO-D-13-099.1.

Saltzman, B., 1957: Equations governing the energetics of the larger scales of atmospheric turbulent in the domain of wave number. *J. Meteor.,* **14,** 513–523, doi:10.1175/1520-0469(1957)014<0513:EGTEOT>2.0.CO;2.

Schott, F. A., L. Stramma, and J. Fischer, 1995: The warm water inflow into the western tropical Atlantic boundary regime, spring 1994. *J. Geophys. Res.,* **100,** 24 745–24 760, doi:10.1029/95JC02803.

——, J. Fischer, and L. Stramma, 1998: Transports and pathways of the upper-layer circulation in the western tropical Atlantic. *J. Phys. Oceanogr.,* **28,** 1904–1928, doi:10.1175/1520-0485(1998)028<1904:TAPOTU>2.0.CO;2.

——, and Coauthors, 2003: The zonal currents and transports at 35°W in the tropical Atlantic. *Geophys. Res. Lett.,* **30,** 1349–1352, doi:10.1029/2002GL016849.

Send, U., C. Eden, and F. Schott, 2002: Atlantic equatorial deep jets: Space–time structure and cross-equatorial fluxes. *J. Phys. Oceanogr.,* **32,** 891–902, doi:10.1175/1520-0485(2002)032<0891:AEDJST>2.0.CO;2.

Stommel, H. M., 1982: Is the South Pacific helium-3 plume dynamically active? *Earth Planet. Sci. Lett.,* **61,** 63–67, doi:10.1016/0012-821X(82)90038-3.

Stramma, L., S. Hüttl, and J. Schafstall, 2005: Water masses and currents in the upper tropical northeast Atlantic off northwest Africa. *J. Geophys. Res.,* **110,** C12006, doi:10.1029/2005JC002939.

——, G. C. Johnson, E. Firing, and S. Schmidtko, 2010: Eastern Pacific oxygen minimum zones: Supply paths and multidecadal changes. *J. Geophys. Res.,* **115,** C09011, doi:10.1029/2009JC005976.

Thierry, V., A.-M. Treguier, and H. Mercier, 2004: Numerical study of the annual and semi-annual fluctuations in the deep equatorial Atlantic Ocean. *Ocean Modell.,* **6,** 1–30, doi:10.1016/S1463-5003(02)00054-9.

von Schuckmann, K., P. Brandt, and C. Eden, 2008: Generation of tropical instability waves in the Atlantic Ocean. *J. Geophys. Res.,* **113,** C08034, doi:10.1029/2007JC004712.

von Storch, H., and F. W. Zwiers, 1999: *Statistical Analysis in Climate Research.* Cambridge University Press, 484 pp.